UiT
THE ARCTIC UNIVERSITY OF NORWAY

universität innsbruck

Faculty of Science and Technology

Department of Physics and Technology

Role of hafnium doping concentration on the structural and surface properties of ZnO surfaces

—

Toni Moser

EOM-3901 Master's Thesis in Energy, Climate and Environment- June 2019

Supervision: Matteo Chiesa and Paul Scheier

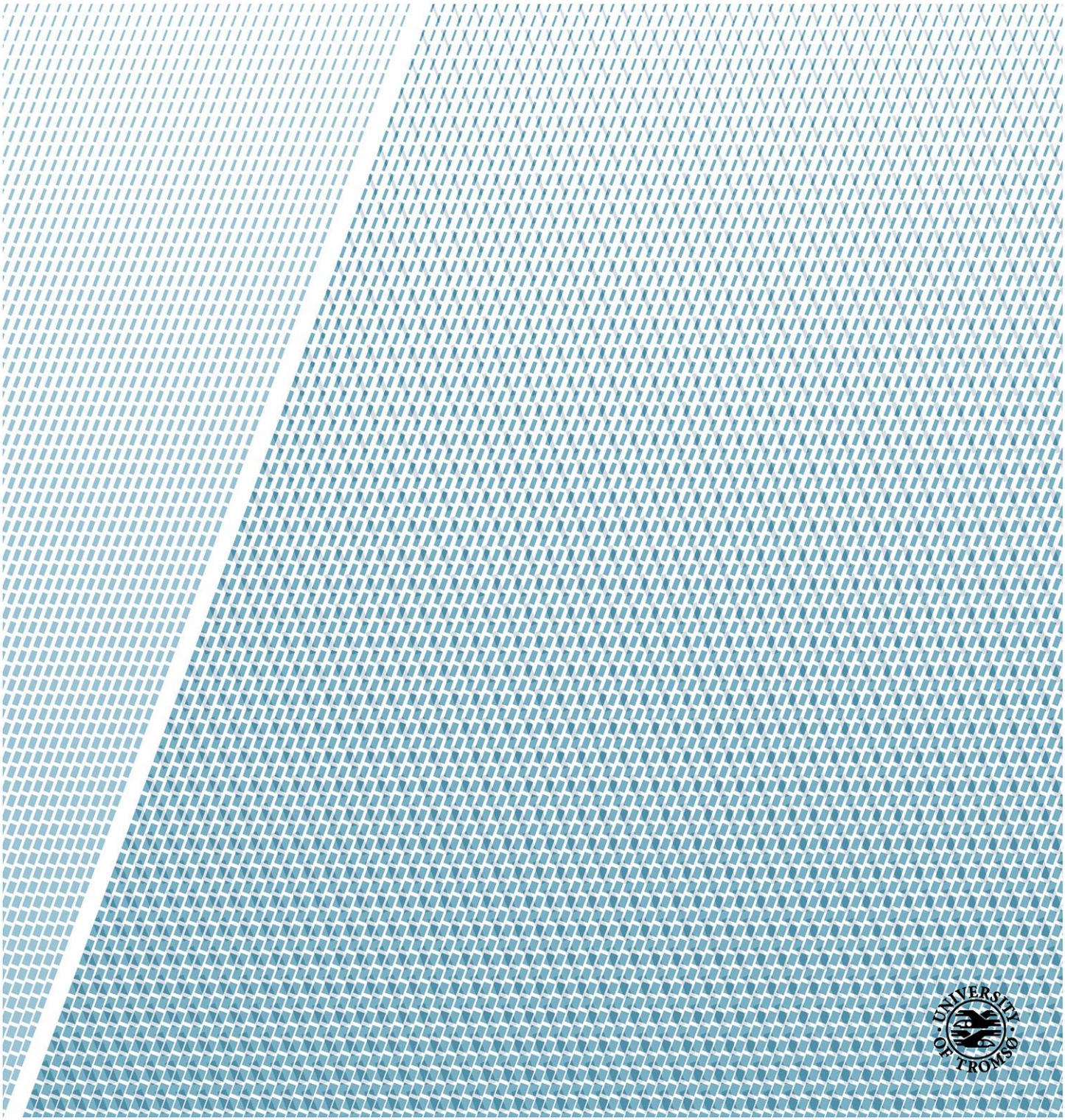

Declaration

I hereby declare and confirm that this thesis is entirely the result of my own original work. Where other sources of information were used, they are indicated as such and properly acknowledged. I further declare that this or similar work has not been submitted for credit elsewhere.

Date: _____

Signature: _____

Dear readers,

this thesis was written as part of my master program in material- and nanosciencee at the University of Innsbruck. The experiments and the writing was conducted during my year abroad in Tromsø, Norway at the University of Tromsø and will be handed in Tromsø as well as in Innsbruck, where I will graduate.

Abstract

The presented thesis deals with the characterisation of hafnium doped zinc oxides with focus on the application as transparent conducting film (TCF) or electron transport layer (ETL) in heterojunction solar cells. Atomic force microscopy (AFM), scanning electron microscopy (SEM), transmission electron microscopy (TEM), electrical and optical methods have been applied to characterise the examined samples with the focus on AFM. Different AFM techniques are presented, conducted on some training samples and finally applied to investigate the evolution of the Hamaker constant in dependence of hafnium doping concentrations in zinc oxide. The thin film samples with a thickness of 75 nm were grown by atomic layer deposition and varying cycle ratios of diethyl-zinc and tetrakisethylmethylaminohafnium were used to control the doping concentrations. It has been shown that the Hamaker constant increases with doping concentration and peaks for a 1:1 cycle ratio and decreases at higher doping concentrations. The same trend has been observed for band gap, carrier concentration and force of adhesion. The reliability of retrieving Hamaker constants via the relatively new method of bimodal imaging method in comparison to using reconstructed force curves is presented. The observed high heterogeneity of the samples is assumed to be caused by polycrystallinity. High-resolution transmission electron microscopy (HRTEM) was able to confirm the polycrystallinity of the samples.

Contents

1 Introduction

The growing global energy consumption and the imminent threat of climate change increase the need for clean and renewable energy sources. While there has been a big rise in the renewable energy sector over the past decade, CO_2 emissions have seen a continued rise in the last years [1]. As the largest exploitable source of renewable energy, solar energy holds tremendous potential. To achieve the goal of a sustainable future, new technologies and materials have to be found to increase efficiencies, lower the production cost, ensure an environmentally friendly and more sustainable production, reduce stress on rare materials and in general increase availability of solar power. Thin film solar cells hold the potential to greatly reduce production cost as well as material consumption. In contrast to conventional crystalline silicon solar cells that use busbars and fingers as front contacts, most thin-film solar cells use transparent conductive films (TCFs) as front contacts. TCFs are used to cover the whole front face of the solar cell, decreasing the path lengths in photoactive material for the charge carriers and thereby increasing the collection rates.

Indium tin oxide (ITO) is widely used due to its excellent optical and electrical properties. Up to this day indium is being harvested as a byproduct of the zinc smelting and refining industry, but indium's rarity poses the risk of a sharp cost increase in the future for ITOs if the demand for indium rises [2]. Zinc oxides have shown promising results to take that role [3–10] and their great abundance and low cost make it especially interesting for the solar industry, since solar cells have to compete with other cheap electrical power sources like coal-, wind- or hydro power. Aluminium doped zinc oxide has been widely studied in silicon-based thin film solar

cells [5–8], among other doping agents [9–11]. In cooperation with members of the Department of Materials Science and Engineering and Department of Microsystems Engineering of Khalifa University in Abu Dhabi, we have shown that hafnium doped zinc oxides is an interesting candidate to take over the role of ITOs and thus reduce the indium demands for thin film solar cell production. Atomic force microscopy (AFM) has been proven to be a powerful characterisation tool and is applied to characterise the hf doped Zno samples. The applied AFM methods and the achieved characterisation results for different hafnium doping concentrations are presented in this thesis.

2 Theoretical background

2.1 Atomic Force Microscopy - AFM

An atomic force microscope (AFM) is a type of scanning probe microscope using a sharp tip to scan the surface of a sample. The principle idea of atomic force microscopy (AFM) was developed after the invention of the scanning tunnelling microscope (STM) by G. Binnig and H. Rohrer in 1982 [12]. The working principles of the two are similar and hence only four years after the invention of the STM the invention of the AFM followed in 1986 [13]. While the STM uses the tunnelling current between a sharp conducting tip (typically metal) and the sample to track the sample surface, the AFM makes use of the atomic forces acting between a tip (typically silicon) and the sample surface.

One major disadvantage of scanning tunnelling microscopy is that the sample has to be conductive, consequently, non-conductive samples have to be coated with a conductive material, which is often not desirable. The search for a method for non-conductive materials ultimately resulted in the invention of atomic force microscopy, where a (not necessarily conducting) tip is placed on a cantilever and is scanned over the sample (fig. 2.1). Attractive and repulsive forces acting between the tip and the substrate lead to bending/deflection of the cantilever. To capture these tiny deflections of the cantilever, a laser is focused on the tip of the cantilever, where it gets reflected and subsequently hits a four-segment photodiode. The photodiode converts the signal to a voltage output that is sensitive to vertical (transverse forces)

as well as horizontal displacements of the cantilever (lateral forces). In this way, small deflections of the cantilever can be detected and converted to reconstruct the topography of the sample. A piezoelectric crystal is used to control the distance between the tip and the sample (z-axis). Two additional piezoelectric crystals control the movement in the x-y-plane. In principle, it is possible that either the tip is moving over the sample surface or that the sample is moved. In most cases, as in our machine, the latter is realised. All experiments were performed using a Cypher AFM with an environmental scanner from *Asylum Research* and standard OLYMPUS cantilevers.

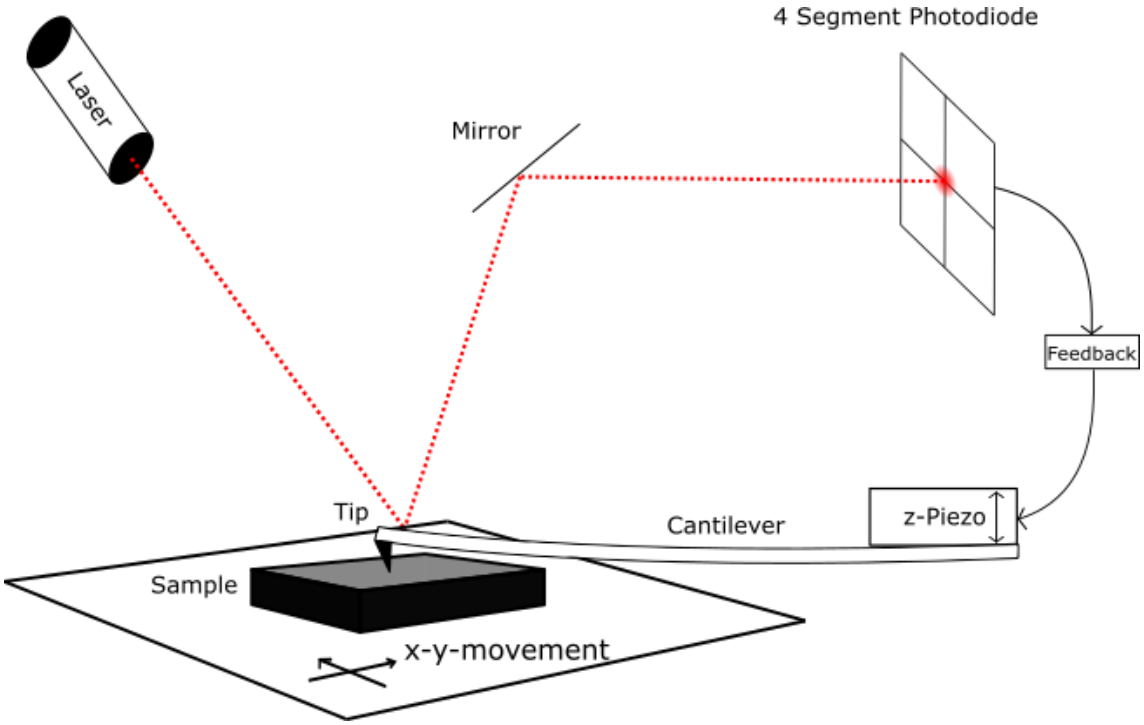

Figure 2.1: Schematic working principle of an AFM. The cantilever is attached to a piezo, controlling the z position. A laser beam is reflected by the cantilever close to the tip and is used to measure the deflection, using a 4 segment photodiode.

2.1.1 Imaging modes

Three different modes of operation are commonly referred to and are widely used. Over the years names and details might have changed but in a general, the following three modes can be described as done below.
The first established mode was the **contact mode**. In this mode, the cantilever is brought into the repulsive regime of the tip-sample interaction (see sec. 2.1.2), also referred to as mechanical contact, hence the name for the mode of operation. It can be considered the simplest mode of operation and its working principle resembles that of a record player. The tip is scanned over the sample surface and its topography leads to the deflection of the cantilever. Most commonly this mode is operated in the constant force mode: The tip is lowered onto the surface until a desired preset deflection is reached. Using a feedback loop, the z-piezo constantly adjusts the height and keeps the deflection of the cantilever constant while the sample is scanned. The second mode of operation is the constant height mode, where the tip is kept at a constant height. The constant height mode is only used for relatively flat samples since it poses the risk of damaging the tip or even breaking the cantilever when height changes become too large. For the constant height mode, this risk is reduced, since the tip follows the surface and is, therefore, more commonly used. Even though still widely used, contact mode is not suitable for many samples, where damages to the sample might occur and more information than plain topography imaging is desired. This is especially a problem for soft materials and features not strongly bound to the substrate, e.g. DNA on mica. In figure 2.2 the displacement and damage of a feature is illustrated as it could occur when using contact mode.

The **non-contact mode** is one of two dynamic modes (see figure 2.3), that sets the cantilever into oscillation by exciting it at or near one of its resonance frequencies. The cantilever is usually placed several nanometers above the sample surface while the amplitude of the oscillation is typically a few nanometers. In this mode,

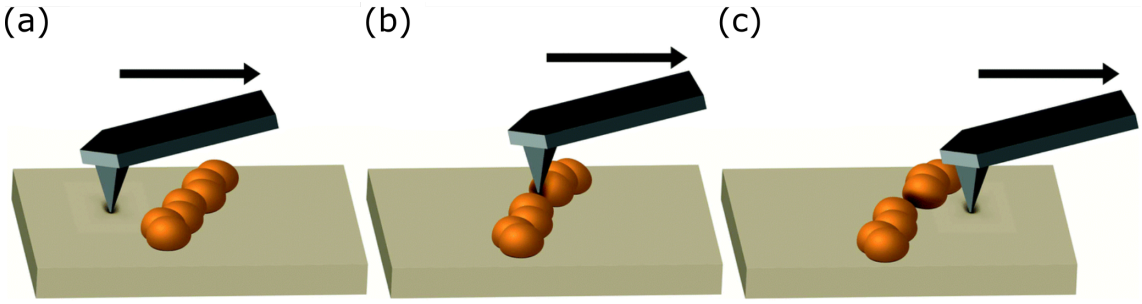

Figure 2.2: Illustration of static/contact mode AFM imaging during its movement from left to right. a, b, and c show a time series of the movement. Damages and/or displacement of features might occur as illustrated in (b). Illustration from thankfully received from [14].

attractive forces dominate and lead to a phase lag greater than 90° [15]. At the beginning of AFM research it was assumed that in this mode no mechanical contact is made and only longer-ranging van der Waals forces act on the tip, hence the name. Today it is clear that mechanical contact can be made, but that the sum of interaction forces during the oscillation cycle is attractive, consequently, this mode is more precisely referred to as **net attractive mode**. To differentiate, the term **'true' non-contact mode** is used to indicate that no mechanical contact is established throughout the whole oscillation cycle.

The net attractive forces lead to a decrease in resonance frequency and thereby to a decrease in amplitude (see section 2.1.4). Either the amplitude or the resonance frequency of the cantilever is used as a feedback signal, referred to as **amplitude modulated (AM-AFM)** or **frequency modulated atomic force microscopy (FM-AFM)**, respectively. In AM-AFM the amplitude and in FM-AFM the frequency is being tracked and held constant. Changes in sample height lead to a change in amplitude/resonance frequency (for a more detailed explanation see section 2.1.4). This signal is used as a feedback signal to keep the tip-sample distance and therefore the amplitude/resonance frequency constant. The mode of operation resembles the constant force mode in contact mode, using the amplitude/resonance frequency as feedback signal instead of the cantilever deflection. Likewise, the topography is reconstructed by monitoring the feedback signal. Historically, the AFM

community has been strongly divided into the AM-AFM and the FM-AFM community and still is to some degree, often leading to the parallel, but more or less independent, development of similar techniques.

Since contact is only made for a very short period of time or not at all (true non-contact mode), tip degradation and sample damaging are less likely, hence this technique is especially useful for soft samples, where sample damage is otherwise likely to occur, e.g. soft biological samples. The longer ranging forces acting on the tip in this mode are comparatively small to the repulsive forces in the contact mode, consequently making it more difficult to achieve similar resolution.

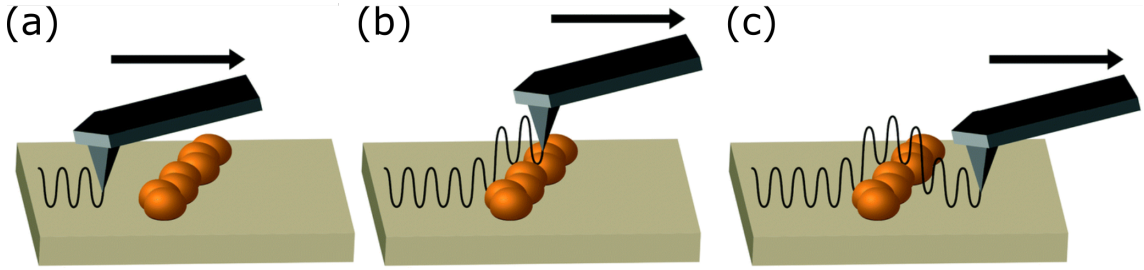

Figure 2.3: Illustration of dynamic (non-contact or tapping mode) AFM imaging during its movement from left to right. (a), (b), and (c) show a time series of the movement. Damages and/or displacement of features are greatly reduced due to reduced lateral interactions and contact time. Illustration thankfully received from [14].

The second dynamic-mode using oscillation of the cantilever is the so-called **tapping mode**. Similar to the non-contact mode the tip is placed above the surface and is excited at its resonance frequency. The oscillating tip is then lowered onto the sample until it makes contact with the sample. Ultimately, the contact leads to a reduction in amplitude. The tip is lowered until a preset reduction of the amplitude is reached. The predefined amplitude is held constant by driving the z-piezo to compensate for topography changes while scanning the sample. Every drive cycle the tip makes mechanical contact with the sample, which can be described as a tapping of the tip onto the sample, hence the name. The sum of tip-sample interaction forces over an oscillation cycle is repulsive, therefore this mode is also referred to **net repulsive**

mode. Tapping mode combines the advantage of greatly reducing damage and displacement of features, which is typical for the non-contact mode while achieving higher resolution by making use of the stronger repulsive forces as in contact mode.

2.1.2 Forces

While optical microscopy is strongly restricted in its resolution limit by the wavelength of the used light, AFM is mainly restricted by the radius of the tip and since tips with less than 10 nm are widely available, resolutions far beyond the optical limits can be achieved.

For a proper interpretation of the generated images, it is invaluable to understand the nature of the contrast that is achieved. To describe the interactions between two particles, the so-called Lennard-Jones interatomic potential

$$U_{\mathrm{LJ}}(r) = 4U_0 \left(\left(\frac{\sigma}{r}\right)^{12} - \left(\frac{\sigma}{r}\right)^{6} \right), \tag{2.1}$$

is widely used, where U_0 is the depth of the potential well, r is the interatomic distance and σ is the distance at which the potential equals zero. In figure 2.4 a Lennard-Jones potential is plotted. The r^{-6}-term describes the attractive longer-ranging interactions caused by van der Waals forces (London Dispersion, Debye and Keeson forces). The r^{-12}-term describes the shorter ranging repulsive interactions caused by Pauli and Coulomb repulsion of the nuclei. The r^{-6}-term is well established and can be theoretically deduced, whereas the r^{-12}-term does not approximate experimental results as well as other potential functions would. The Lennard-Jones potential is one of many different potentials describing the interaction of two particles and is not considered one of the most accurate, but its simplicity makes it widely used. Since the focus in the further deduction lies on the attractive part, it will suffice for the analysis done in this thesis.

In 1937 Hamaker used van der Waals force to approximated the attractive forces

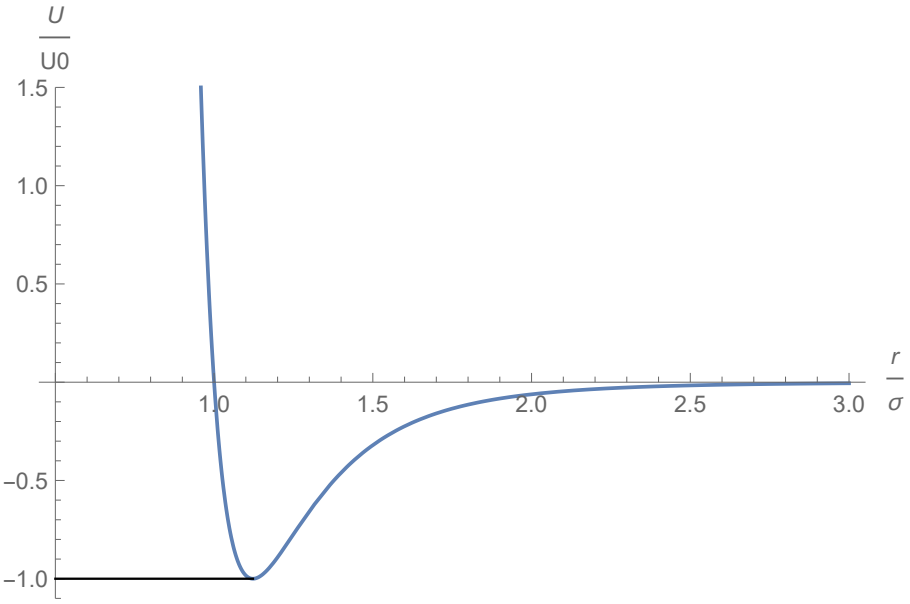

Figure 2.4: Lennard-Jones interatomic potential described by equation (2.1). Plot created using *Wolfram Mathematica*.

acting between two spheres consisting of atoms, by adding up the forces acting between each atom of the two spheres [16]. Using his results the potential U_{ts} between the tip (approximated by a sphere) and the sample surface (approximated by an infinitely large plane/sphere with infinitely large radius) can be calculated as

$$U_{\text{ts}} \approx -\frac{HR_{\text{tip}}}{6d}, \tag{2.2}$$

$$H = \pi^2 C \rho_1 \rho_2, \tag{2.3}$$

where R_{tip} is the tip radius, d is the tip-sample distance, H is the so-called Hamaker constant (also referred to as "the Hamaker"), ρ_1 and ρ_2 are number densities of the interacting particles and C is the coefficient of particle-particle interaction. Since the force is the negative gradient of the potential,

$$F_{\mathrm{ts}} \approx -\frac{HR_{\mathrm{tip}}}{6d^2}, \tag{2.4}$$

where F_{ts} is the force acting between the tip and the sample. The strongest attractive force measured is the so-called force of adhesion F_{AD} and is defined as the minimum of the force-distance profile. It describes how strongly the tip is bound to the sample and relates to the surface energy γ_{TS} as [17]

$$F_{\mathrm{AD}} = 4\pi R_{\mathrm{tip}}\gamma_{\mathrm{TS}}. \tag{2.5}$$

Changes in F_{AD} are directly linked to changes in surface energy, assuming R_{tip} is constant. .

Lifshitz developed a more accurate description of the interaction including dielectric properties in the mid-1950s [18]. As pointed out in [19] equation (2.2) and (2.4) remain unchanged, but the calculation of the Hamaker constant changes and therefore the information that can be obtained if the Hamaker constant is measured is a different one. Lifshitz theory does not use pairwise additivity as Hamaker did but uses bulk properties to describe the interaction. In this approach the Hamaker constant in (2.2) and (2.4) takes London dispersion (frequency dependent) forces, Keesom (permanent) and Debye (permanent induced) dipoles into account [19].

2.1.3 Spring-Mass Model

The simplest model to describe a cantilever-tip system is the spring-mass model as shown in figure 2.5. It is an example of an harmonic oscillator and therefore the relation

$$\omega_0 = \sqrt{\frac{k}{m}} \tag{2.6}$$

applies, where k is the spring constant/stiffness of the cantilever, M is the mass and ω_0 is the resonance frequency. Introducing a dampening parameter b, governing equation of motion is given by

$$m\frac{d^2z}{dt^2} + 2b\frac{dz}{dt} + kz = F_{\mathrm{D}}(t) \tag{2.7}$$

where z is the position of the tip relative to its unperturbed equilibrium position and $F_{\mathrm{D}}(t)$ is the driving force. Instead of the dampening the so-called quality factor or Q factor, defined as

$$Q = \frac{\omega_0}{\Delta\omega}, \tag{2.8}$$

where $\Delta\omega$ is the resonance width or full width at half maximum, can be used. The higher and narrower a peak, the larger its Q factor. For cantilevers used for this thesis, Q values between 100 and 400 were typical. Using (2.7) one can deduce the amplitude response $A(\omega)$ to a sinusoidal driving signal with driving force amplitude F_{D_0} and frequency ω, given by

$$A(\omega) = \frac{F_{\mathrm{D}_0}}{\sqrt{(k - m\omega^2)^2 + 4b^2\omega^2}}. \tag{2.9}$$

The spring-mass model might appear like an oversimplification and indeed it is not capable of explaining the higher resonant modes of the cantilever, while it is sufficient for most considerations done in this thesis. By adding springs in series, higher modes can also be described. For a deeper understanding of the higher modes, more rigorous considerations must be made as it is done in beam theory[20].

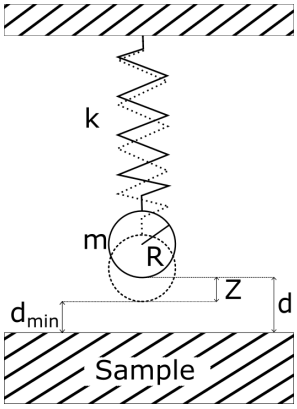

Figure 2.5: Spring-mass model of the cantilever-tip-sample system.

2.1.4 Effects of forces on cantilever

A cantilever is typically characterised by its stiffness k, its resonance frequency ω_0 and its quality factor Q. When the cantilever approaches the surface of a sample the tip-sample interaction can change the effective values of the cantilever. One of the easiest approximations[21] is that the cantilever stiffness is replaced by an effective cantilever stiffness k_{eff}. The effective cantilever stiffness is given by

$$k_{\text{eff}} = k - F', \tag{2.10}$$

where k is the stiffness of the unperturbed cantilever and F' represents the sum of force derivatives acting on the tip. The effective resonance frequency ω_{eff} changes according to (2.6) to

$$\omega_{\text{eff}} = \sqrt{\frac{k_{\text{eff}}}{m}} = \omega_0 \sqrt{1 - \frac{F'}{k}}. \tag{2.11}$$

In the case of a net repulsive force acting on the tip ($F' < 0$) then $\omega_{\text{eff}} < \omega_0$ whereas if a net attractive forces acts on the tip ($F' > 0$) then $\omega_{\text{eff}} > \omega_0$. In figure 2.6 equation (2.9) is plotted for different values of k due to net attractive/repulsive forces.

When a cantilever driven with $\omega = \omega_0$ approaches the sample surface it experiences

a net attractive force (fig. 2.6 orange) leading to a reduction in amplitude. The same applies for a net repulsive force (fig. 2.6 green). The approximation done in equation (2.10) is only applicable if $|F'| \ll k$, but in the calculation done for figure 2.6 a ratio of $|F'/k| = 0.05\%$ was used and already a reduction in amplitude of roughly 33% is achieved. Therefore the approximation can be assumed to be reasonable. In the approximation used for figure 2.6 it is assumed that F' is constant for each curve, while in reality F' is dependent on the amplitude itself, since a larger amplitude also implies that the tip is getting closer to the surface, whereas for a small amplitude the cantilever will experience a nearly negligible force. As a result real amplitude response curves look differently and in general more complicated as shown in [22].

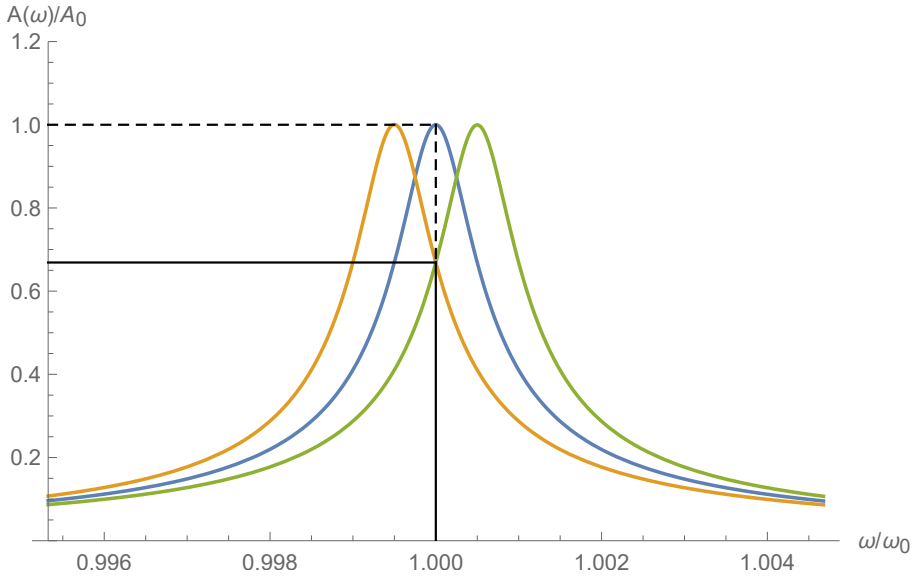

Figure 2.6: Amplitude response for a unperturbed (blue) cantilever ($Q = 640$), experiencing a net attractive ($F'/k = 0.05\%$) force (orange) and experiencing a net repulsive ($F'/k = -0.05\%$) force (green), leading to different k_{eff}-values. Note: The amplitude values for the orange and the green line at $\omega/\omega_0 = 1$ are only approximately equal. Plot created using *Wolfram Mathematica*

2.1.5 Phase contrast image

In AM-AFM the amplitude A_1 of the cantilever is used as the feedback signal and to reconstruct the topography of the sample. If the AFM is working well and the gains are set correctly the amplitude signal should not bear any information about the sample, since it should be constant and equal to the setpoint A_{SP}, except for noise. The integral gain is the tuning parameter typically used to control the response of the z-piezo to the feedback signal. It has to be adjusted according to the scan rate, where higher scan rates require a higher integral gain. If the integral gain is set to low, the tip is "parachuting off" of high features, meaning that it is not able to follow the surface and the tip-sample distance increases. This is typically coupled with getting closer to the surface when going up on features. In both cases the amplitude and phase will change, leading to amplitude and phase contrast. Phase contrast might be interpreted as a variation in material properties but is, in reality, a result of a badly set integral gain.

It is not possible to distinguish if the AFM is working in the net repulsive or net attractive regime, just by looking at the amplitude signal alone (an experienced AFM user might still be able to make an educated guess due to the ratio of free unperturbed amplitude A_{01} to A_{SP}). However, it is easy to distinguish these two cases, but also gain more information, with the use of the phase ϕ_1-channel. Note that in this thesis, the phase lag is considered, so if the phase angle is becoming larger, this corresponds to a greater phase lag. To understand the meaning of the phase the considerations of Magonov et al. [22] are followed, with some sign adaptions to be consistent within this thesis.

The phase angle ϕ can be calculated by

$$\phi(\omega) = tan^{-1}\left(\frac{m\omega\omega_0}{Q(k - m\omega^2)}\right). \tag{2.12}$$

When the cantilever is driven at its resonance frequency $\omega = \omega_0$ the phase lag is $\phi = 90°$, when it is driven below ($\omega < \omega_0$) the phase lag is smaller $\phi < 90°$ and

$\phi > 90°$ for $\omega > \omega_0$. The vibrational characteristics of the cantilever change due to tip-sample interactions as described in section 2.1.4 and in [21, 22]. Using the previous approximation the phase angle shift $\Delta\phi_0$ at ω_0 can be approximated [22] as

$$\Delta\phi_0 = tan^{-1}\left(-\frac{k}{QF'}\right) - 90° \approx \frac{QF'}{k}, \tag{2.13}$$

where the approximation holds for $F' \ll k$. Since Q and k are always positive values, the phase angle shift coincides with the overall force derivative F'. A net attractive force, having a positive F', leads to a positive phase shift $\Delta\phi_0 > 0$ and phase angle above $\phi(\omega_0) =: \phi_0 > 90°$, whereas a net repulsive force ($F' < 0$) leads to a negative phase shift $\Delta\phi_0 < 0$ and therefore to a phase angle lower than $\phi_0 < 90°$. It is further possible to use variation in phase angle as a measurement of energy dissipation ([23] and equation (2.15)) and adhesive interaction [24] variations on the sample in tapping mode.

2.1.6 Force reconstruction

The simplest form of force measurement is done in the so-called dc-mode by "pressing" the tip onto the sample and monitoring the deflection as a function of tip-sample separation [25]. Since the deflection is proportional to the force applied to the cantilever, the transformation from deflection to tip-sample interaction force F_{ts} is rather simple. The lack of capability to achieve compositional contrast due to dissipative mechanisms [26–28] or conservative interactions while imaging [29] and a higher $1/f$ noise factor [27, 30] are major disadvantages of the dc operation, which can be overcome by dynamic AFM [31]. The equation of motion for the tip in

proximity to the sample is given by[15]

$$\frac{d^2z}{dt^2} + \frac{m\omega}{Q}\frac{dz}{dt} + kz = F_{\mathrm{ts}} + F_{\mathrm{D}} \tag{2.14}$$

where F_{ts} is the force between the tip and the sample and Q is the Q factor due dissipation with the medium. This is just small adaption of (2.7) for the driven damped harmonic oscillator. The tip sample distance d is given by $d = z_{\mathrm{c}} + z$, where z_{c} is the tip-sample separation (z as before)[15]. From (2.14) the dissipated energy[32]

$$E_{\mathrm{dis}}(d) = \frac{\pi k A_{01} A_1(d)}{Q}\left(sin\left(\phi_1(d)\right) - \frac{A_1(d)}{A_{01}}\right) \tag{2.15}$$

can be derived. To reconstruct the force (F_{ts}), the amplitude A_1 and phase ϕ_1 curves versus separation distance d upon approach and retraction are recorded. To convert these curves to force F_{ts} versus minimum separation distance $d_{\mathrm{min}} \approx z_{\mathrm{c}} - A$, the Sader-Jarvis-Katan formalism [30, 33]

$$F^*_{\mathrm{ts}}(d) = \frac{2k}{|F_{\mathrm{AD}}|}\int_{u=d}^{u=\infty}\left[\left(1 + \frac{A_1^{1/2}}{8\sqrt{\pi(u-d)}}\right)\Omega(u) - \frac{A_1^{3/2}}{\sqrt{2(u-d)}}\frac{d\Omega(u)}{du}\right]du \tag{2.16}$$

is used, where Ω is the normalised frequency shift expressed by

$$\Omega(d) = \left[1 + \frac{A_{01}}{QA_1}cos(\phi_1(d))\right]^{1/2} - 1. \tag{2.17}$$

The separation distance at $F_{\mathrm{ts}} = F_{\mathrm{AD}}$ is set to zero ($d = 0$). It is required that the force transition from attractive to repulsive regime occurs smoothly and that bi-stability is avoided as explained in the next section. A more detailed explanation of the method used to recover the force can be found in [31] and [34]. The reconstructed force curves can be used to to distinguish between different materials due to specific

shape of each material [35] and the retrieved force of adhesion can be used to draw conclusions about the wetting behaviour at an microscopic scale [36, 37].

2.1.7 Critical amplitude

To be able to reconstruct the force according to section 2.1.6 a smooth transition from attractive to repulsive regime must be established as well as avoiding bi-stability [38–40]. Since there is no universal numeric value for the amplitude that can be used, other methods are required to ensure a smooth transition, which can be done by determining the so-called critical amplitude A_C [41]:
For sufficiently small free amplitude values i.e. typically $A_0 < 2 - 5\,\mathrm{nm}$, mechanical contact is never established and the tip only operates in the attractive regime[42], see figure 2.7 (a) . In this regime, the phase lag is always greater than 90°. As the amplitude A_0 is increased and reaches a critical value, the cantilever snaps into mechanical contact (phase lag less than 90°) on approach and snaps out of it during retraction, see figure 2.7 (b). These discrete jumps lead to a loss of information due to the sudden change of d. The snapping in and out of the cantilever does usually not occur at the same distance d and the AFM community, therefore, speaks of a bi-stable behaviour or bi-stability [43]. The snapping out typically appears at greater distances since short-ranged adhesive forces keep the cantilever from retracting until the force becomes too large, while on approach the cantilever has to approach close to the surface before the forces become strong enough for the cantilever to snap in. The so-called critical amplitude A_C is the mean value of amplitudes A_0 for which a discrete transition is observed [41]. The smallest amplitude A_0 where the discrete transition can be observed is referred to as the minimum critical amplitude A_{Cm}. The critical amplitude is sensitive to tip size (sec. 2.1.8), cantilever stiffness and material properties. Increasing the amplitude to around twice the critical amplitude, a smooth transition from attractive to the repulsive regime is established [38, 42], as shown in figure 2.7 (c).

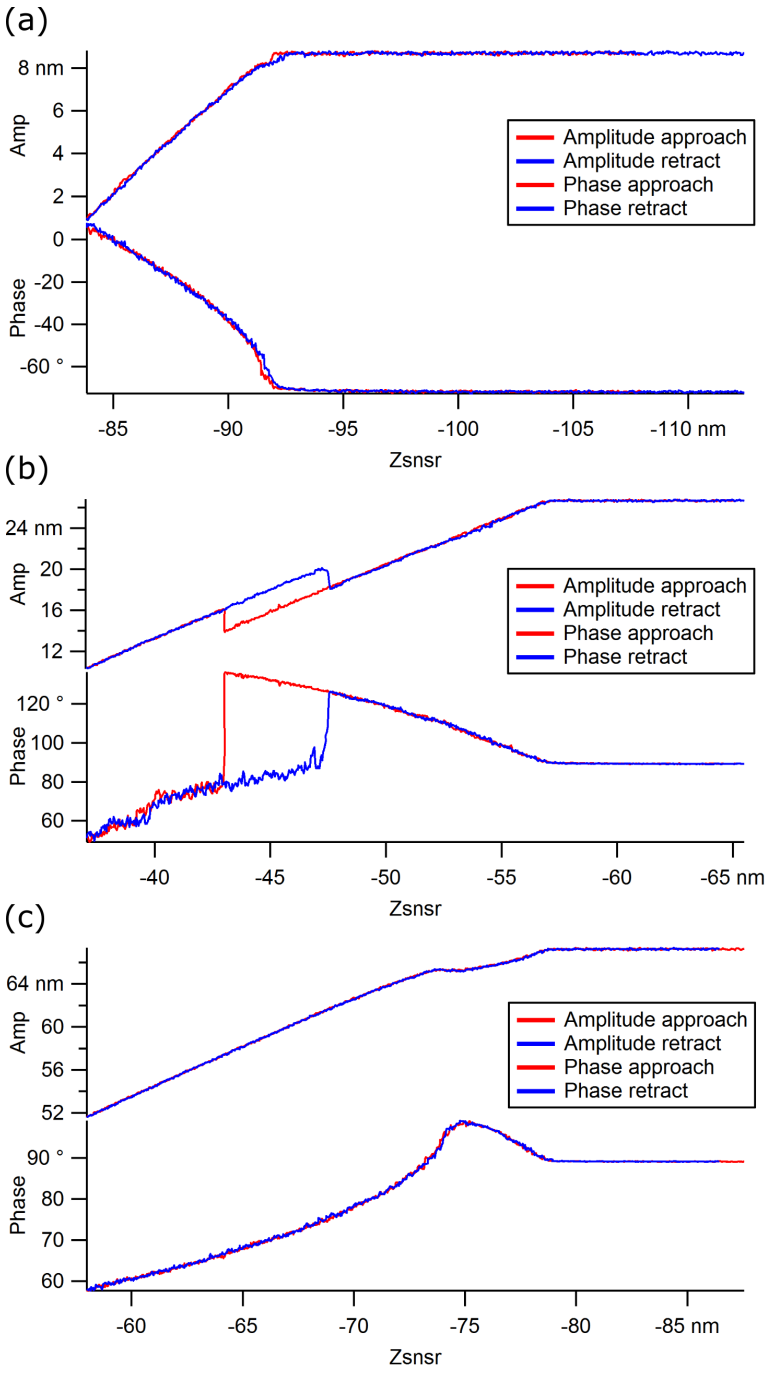

Figure 2.7: Amplitude A_1 and phase ϕ_1 versus distance curves taken on an highly oriented pyrolytic graphite (HOPG) sample with increasing $A_0 1$ from (a)-(c): (a) only net attractive forces act throughout the whole approach and retraction, (b) discrete transition from attractive to repulsive with bi-stable behaviour, (c) smooth transition from attractive to repulsive regime.

2.1.8 Calibration

Achieving quantitative results, besides topographic (height and size of features) measurements, has been shown to be a challenging task with AFM. To accurately measure physical quantities like the force of adhesion, Hamaker constant or stiffness, some physical properties of the tip and the cantilever must be well known. Techniques to estimate the tip radius in situ without damaging the tips have been proposed by [44] and are used to monitor tip radius during measurements. It is crucial to drive the cantilever at the resonance frequency to be able to accurately reconstruct the tip-sample interaction force. To accurately calibrate the drive frequency *Asylum Research* offers different techniques, including a thermal calibration used for the measurements described in this thesis.

Tip size estimation

Since most experimental observables of atomic microscopy are influenced by the tip radius, it is crucial to be able to estimate the tip radius to perform quantification measurements. It is desirable for the estimation to be done *in situ* and without risk of damaging or contaminating the tip. Such a technique was suggested by Santos et al. [42] and confirmed by Maragliano et al. [44]. It uses the minimum critical amplitude A_{Cm} to estimate the tip radius R_{tip}. They propose the relation

$$A_{\mathrm{Cm}} = K R_{\mathrm{tip}}^{\alpha} \tag{2.18}$$

where K is a constant depending on cantilever and sample properties and α is a fitting parameter. This relation ensures that as long as constant values for A_{Cm} are measured, the tip radius is constant.

Thermal calibration

To reconstruct the force we assume that the cantilever is driven at its resonance frequencies $f_n = \omega_n/2\pi$, where n is the corresponding eigenmode of the cantilever. As seen in figure 2.6 the amplitude is highly sensitive to the drive frequency, therefore f_n must be well known. The values provided by the manufactures are by far not precise enough to achieve reasonable results. To calibrate f_n a thermal calibration technique described in [45] is used. The cantilever is held in place to let it oscillate freely without externally exciting it. Thermal movements excite the cantilever and let it vibrate thermally which can be observed via the deflection signal. Utilising Fourier transformation, the signal is fitted to extract f_n and Q_n, where Q_n is the Q factor of the n^{th} mode. Furthermore, *Asylum Research* provides a thermal calibration function, that additionally provides the stiffness of the cantilever and the conversion factor from amplitude in volts to amplitude in nanometer. To achieve accurate parameters, this calibration is typically conducted between 30 nm and 50 nm above the surface [46, 47].

2.1.9 Bimodal Amplitude Modulated Imaging

This introduction to bimodal AM-AFM follows the review of Santos et al. [14]. When the AFM was first proposed in 1986, the advantages of oscillating the tip were already recognised [13]. Since then many powerful AFM techniques have been developed and the imaging modes described in section 2.1.1 became far more advanced. From the quasi-static operations in the early days, the first dynamic methods arose [48–50] and were recognised as powerful tools improving resolution, sensitivity [51] and lowering the risk of damaging the tip and sample [52]. It became clear that higher modes can also be excited and have to be taken into consideration. At first, techniques were developed that would excite the higher modes by "hammering" [53] the cantilever onto the sample (see fig. 2.8), similar to hitting an object with an iron bar. If the object is rigid, one will feel the vibrations of the metal bar in one's

hand, whereas if the object is soft hardly any vibration will be felt. In the same way, the excitation of higher modes could be used to get information about the sample.

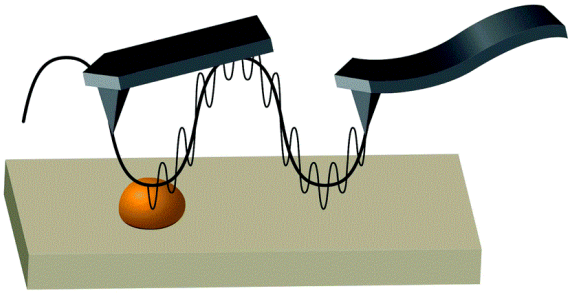

Figure 2.8: The sample is scanned while the tip is oscillated, upon hitting the hard orange feature a higher mode is excited by transferring energy from mode to the other. Illustration thankfully received from [14]

However, this technique of "hammering" onto the sample defeated the purpose of soft interactions to image soft matter [54, 55], which led to the technique of directly and externally exciting the cantilever with two frequencies simultaneously (see fig. 2.9) [56]. This became known as multifrequency AFM in AM mode and enabled imaging with enhanced sensitivity to sample properties even with gentle interactions [14].

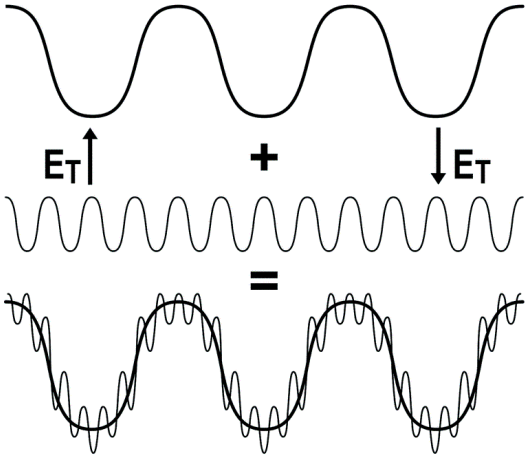

Figure 2.9: Illustration of excitation signal in bimodal imaging. Two frequencies are used to excite two modes of the cantilever. The coupling of the two modes enables the possibility of energy being transferred from one mode to the other. Illustration thankfully received from [14]

The two externally excited modes can couple and transfer energy between modes

well before mechanical contact with the sample is made. As a result higher resolution can be achieved in bimodal non-contact imaging [56, 57]. Having a second frequency signal provides two additional channels, namely the amplitude A_2 and phase ϕ_2 of the second mode. This enables the possibility to use the amplitude A_1 of the first frequency as a feedback signal to control the z-position while the second frequency can be used to track the sample properties [14]. In the case of single frequency AM-AFM, the amplitude signal should hold no information about the sample properties since it is used as the feedback signal and should be constant. Any variation in the amplitude signal can be interpreted as an error signal since it gives the deviation of the pre-set value (setpoint $A_{\mathrm{SP}} \approx A_1$).

Kawai et al. [57, 58] of the FM community proposed that the average derivative of the tip-sample force is the major influence on the higher driven frequency. Their approximation,

$$F' = 2\frac{k_2 \Delta f_2}{f_2} \tag{2.19}$$

with F' the average force derivative over a fundamental cycle dependent on the distance z (as in section 2.1.4), k_2 the stiffness of the second cantilever mode, Δf_2 the shift in resonance frequency of the second mode and f_2 the resonance frequency of the second mode of the unperturbed cantilever (also called free resonant frequency). Equation (2.19) was used to map material properties such as effective Young modulus of proteins [59] and further on led to a closed-form solution in FM-AFM for effective Young modulus, sample-deformation, and viscosity [60]. Since then, a wide variety of contrast maps have been established via bimodal imaging. Lai et al. [61] have shown that it is possible to map the Hamaker constant via bimodal AM-AFM imaging. The method presented by them is used to retrieve Hamaker constants and Hamaker maps via bimodal imaging in this thesis.

In addition it is possible to retrieve force of adhesion maps via the method referred to as bimodal SASS [62, 63]. The cantilever is oscillated with small amplitude (typically

$A_{01} \leq 1\,\mathrm{nm}$) close to the surface (small setpoint), hence the name small amplitude small setpoint (SASS). The cantilever oscillated in close range to the distance of the force minimum as shown in 2.11. Since the force minimum is the equivalent to the force of adhesion and the oscillation is so small, the force of adhesion can be directly obtained from the mean deflection Z_0 and the spring constant of the first mode k_1 as [63]

$$F_{\mathrm{AD}} \approx k_1 z_0. \tag{2.20}$$

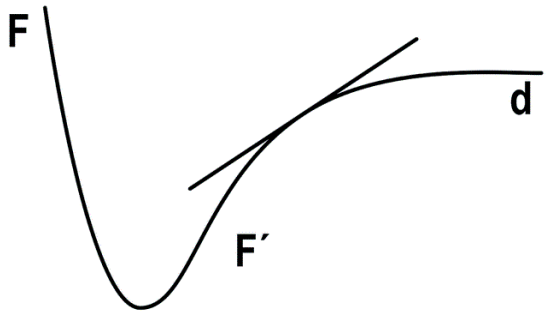

Figure 2.10: The second mode in bimodal AFM is influenced by the derivative F' of the tip-sample interaction force. Illustration thankfully received from [14].

2.2 Solar cells

A solar cell in its most basic form is a diode that is capable of transforming the energy of light into usable electrical energy. It can only transform light with energy greater than its band gap ($E_\nu > E_{\mathrm{G}}$), light with lower energy is either transmitted, reflected or absorbed and leads to the heating of the solar cell. Incoming light with $E_\nu > E_{\mathrm{G}}$ is absorbed and an electron-hole-pair is created, separated at the p-n-junction and collected by the front and rear contact. Crystalline silicon solar cells are the most common solar cells on the market but other technologies and materials have the potential to be superior due to lower cost and resource usage, better carbon

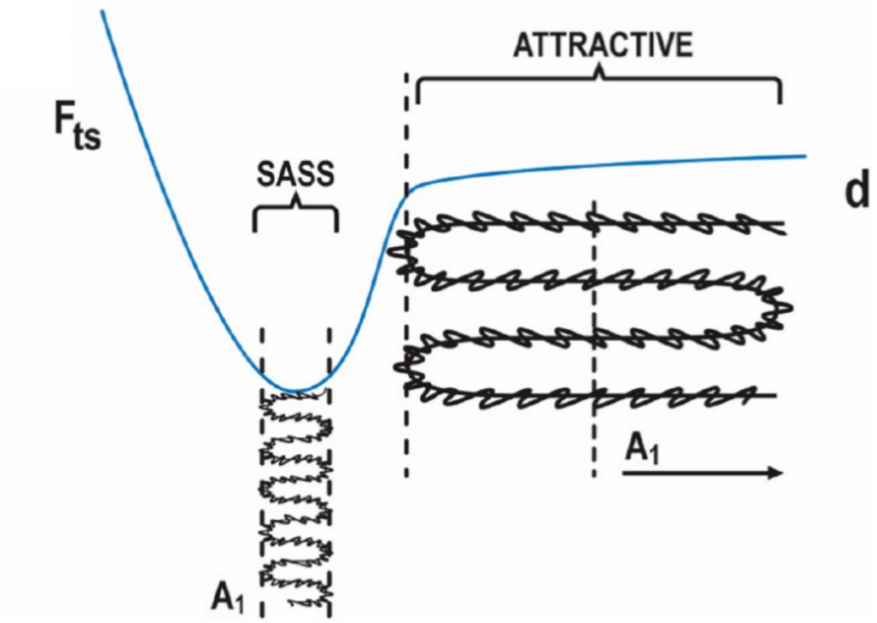

Figure 2.11: Operating modes attractive and bimodal SASSS. Illustration thankfully received from [63]

.

footprint, higher efficiencies and other factors.

Simply speaking, a crystalline silicon solar cell consists of p- and n- doped silicon and a front and rear contact (fig. 2.12). In the transition region from p- to n-doping the so-called p-n-junction is capable of separating the charge carriers. Most commonly the front contact is a grid of so-called fingers and busbars (fig. 2.12 (a)) made out of silver and the rear contact made out of aluminium covering the whole backside. Since most metals are highly reflective, the area covered by the fingers and busbars does not contribute to the generation of electrical power and therefore lowers total efficiency. Consequently as little as possible coverage by the front contacts is desirable, hence a highly conducting material like silver is used for the fingers and busbars. The choice of different material for the rear contact is simply due to the lower cost of aluminium. It should be mentioned that there are newer "bifacial" systems, where the solar cell can also utilise light that is coming from its backside. In that case, the backside cannot be fully covered by a highly reflective metal and a finger and busbar contact is also used on the backside.

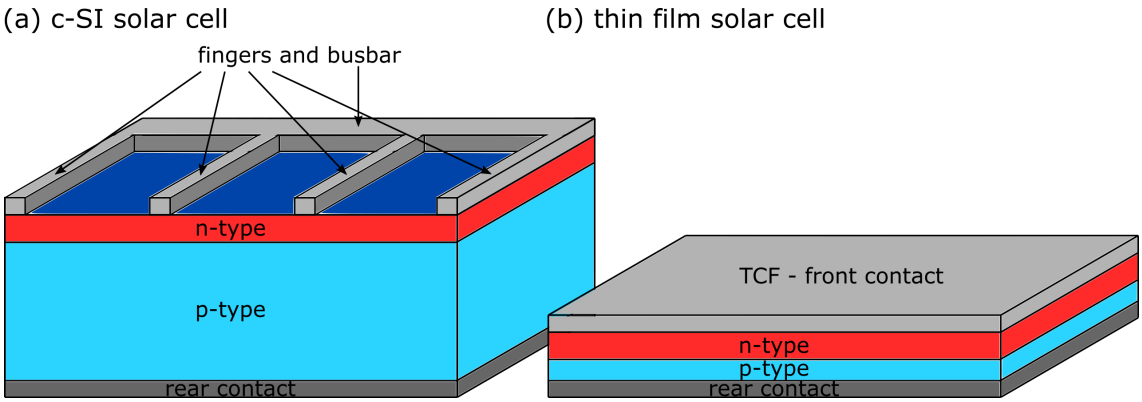

Figure 2.12: schematic drawing of a) a crystalline silicon solar cells using fingers and bus bar b) a thin film solar cell using a TCO as front contact

Thin film solar cells are an alternative to crystalline silicon solar cells, that have the potential of greatly reducing production cost, material usage and energy requirement for production. It is crucial that ratio of the energy output over a lifetime to the energy invested is as high as possible [64] and thin film solar cells show great potential in this regard. Amorphous silicon is the most popular material for thin solar cells [65], partly due to the great abundance of silicon. The illustration shown in figure 2.12 (b) shows a simplified thin film solar cell, but more complex systems using hetero- and multijunctions have been established and have shown higher efficiencies [66]. For most thin film solar cells, recombination losses in the active materials are too high to achieve reasonable efficiencies if a conventional finger and bus bar system is used. Fingers and busbars would need to be placed in close proximity to each other but this is accompanied with high reflection losses caused by the highly reflective bus bars and fingers covering a substantial front area. Therefore most thin-film solar cells use a transparent conducting film (TCF) as front contact (fig. 2.12 (b)). which are transparent and electrically conductive, hence can be used to cover the entire front of the solar cell, achieving higher efficiencies by reducing collection losses without the increase of reflection losses. In most cases, the TCF also works as an anti-reflection coating (ARC) limiting the variability of film thickness (typical ARC thickness is approximately 80 nm). While the resistivity of the TCF might be small

compared to the material used in the photoactive layer, they cannot compete with the low resistivity of silver, therefore combinations of a TCF layer and metal/silver front contacts can be used to enhance efficiency [67].

Most commonly transparent conducting oxides (TCO) are used and out of this category, the most common one is indium tin oxide (ITO). Due to its low resistivity and high transmissivity, it is used widely in electronic and optoelectronic applications. Due to its rarity indium might see a sharp cost increase in the upcoming years [2] if ITO continues to take the role as front contact in thin film solar cells, which could make the front contact a major contributor to material cost. Cheaper alternatives with similar properties, that are more abundant and can be harvested and processed in an environmentally friendly way, are searched for. Zinc oxide (ZnO) offers an alternative and could take over the role of the front contact in thin film solar cells. Not only as front contact, but also as an electron transport layer [68–70] or as an active n-layer in a heterojunction cell [11], ZnO has found its application.

3 Measurements

In order to train and get accustomed to the AFM several experiments were conducted, partially reproducing the results presented in [71] and partially conducting experiments in cooperation with other groups like the liver cell images presented in section 3.2. Two of these practice measurements are presented and discussed briefly.

3.1 Surface Ageing of Graphite

Setup and sample preparation

The first training object was HOPG since it is a relatively simple sample and can be easily cleaved by the scotch tape method. In this method, scotch tape is used to peel off the top layers of an HOPG sample to create a fresh and clean surface. To demonstrate the capabilities of the used instrument some of the measurements in [71] and [72] were repeated. The aim of the measurement is to observe the surface ageing of graphite exposed to ambient air. Surface ageing describes the process of the formation of a film on the surface by airborne contaminants and water. It even has been reported that the formation of the film can lead to the disappearance of features [73]. The temperature, humidity, and pressure are unknown but the experiments were conducted during the month of March in Tromsø, Norway, where the air is typically very dry and the temperature can be assumed to be room temperature (approximately 22 °C). The AFM was used in single frequency AM mode to oscillate the tip at its first resonance frequency. The thermal calibration was performed at a

distance of 30 nm after cleaving the sample and before the first amplitude and phase curves were recorded. Furthermore, it is vital to preserve the tip radius throughout the measurement to obtain any quantitative and comparable results. To preserve the tip and to ensure undisturbed surface ageing, the drive amplitude and therefore the free amplitude were drastically reduced during waiting times but otherwise, the AFM was left turned on and everything left in place, to make as few changes to the system as possible. The tip radius was monitored with the minimum critical amplitude method described in section 2.1.8, whereby the actual tip radius was not of interest but only the preservation of the tip. The first measurement was conducted ten minutes after cleaving, since the loading of the sample, tip approximation, and calibration of the cantilever take some time and have to be done after the cleaving of the sample. The first measurement is referred to as the 0h-measurement and further measurements, conducted one, three, six and twenty-four hours later, are referred to as the 1h-, 3h-, 6h-, and 24h-measurement respectively. A twelve-hour measurement as in [71] could not be conducted due to access restrictions during the night. Each measurement consists of 100 amplitude and phase curves on each sample. A standard OLYMPUS AC160TS-R3 cantilever was used with typical values of $k \approx 26\,\mathrm{N/m}$, $f_1 \approx 300\,\mathrm{kHz}$, $R_{\mathrm{tip}} \approx 7\,\mathrm{nm}$ and $Q \approx 400$. A_{Cm} is material dependent and thus cannot be given as a general cantilever property without the sample type. For the tip used in this measurement cycle $A_{\mathrm{Cm}} = 7.3(7)\,\mathrm{nm}$ on the freshly cleaved graphite surface.

Results and discussion

The tip is assumed to be preserved during the measurement since $A_{\mathrm{Cm}} = 7.3(7)\,\mathrm{nm}$ on a freshly cleaved graphite before the first measurement and $A_{\mathrm{Cm}} = 7.6(7)\,\mathrm{nm}$ after the last measurement on the 24 hours exposed surface. The force was reconstructed via the Sader-Jarvis-Katan[30, 33] formalism as described in 2.1.6 and the results are shown in 3.1 and 3.2. The force profile widens with time which is an indication for a growing water layer on the graphite surface [71, 72]. The force of adhesion

decreases in absolute values for the first six hours and shows a small increase after 24 hours. Whether the increase in force of adhesion after 24 hours is real or due to the measurement uncertainty cannot be confirmed at this time. Since it can be assumed that the tip was preserved during the measurement, the change in $|F_{\mathrm{AD}}|$ can be directly linked to change in surface energy (equ. (2.5)) and surface wettability. The trend in surface energy reduction is expected since an isolated system will attempt to minimise its energy (principal of minimum energy) and has also been simulated by density functional theory (DFT) calculations [72]. The wetting of graphite is closely related to the wetting of graphene that has been studied widely [47, 74–77]. Kozbial et al. reported a higher wettability (corresponding to larger $|F_{\mathrm{AD}}|$) within the first 10 seconds after cleaving and an increase in contact angle (corresponding to smaller $|F_{\mathrm{AD}}|$) after exposure to ambient air [78]. They relate the observed behaviour to the contamination by airborne hydrocarbons. The contamination by hydrocarbons has also been observed by [71] but the formation of the water film seems to occur on a lot larger time scales.

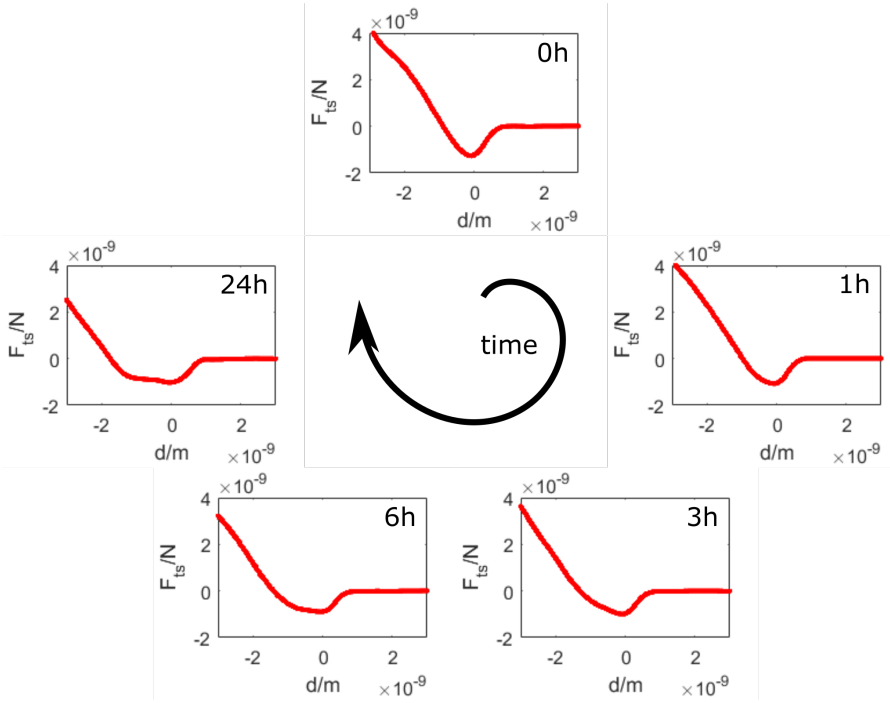

Figure 3.1: Reconstructed force F_{ts} vs distance d curves of graphite exposed to ambient air after 0, 1, 3, 6, and 24 hours.

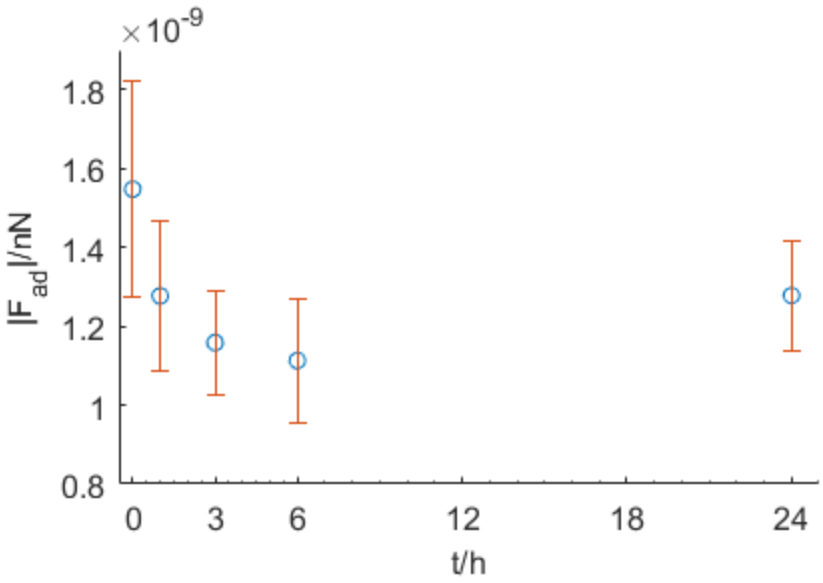

Figure 3.2: Force of adhesion $|F_{\mathrm{AD}}|$ vs time of a graphite sample, error bars are the standard deviations

3.2 Liver cells

In cooperation with another group investigations of fixed and dried liver cells on glass were conducted. The samples were previously treated with osmium tetroxide for SEM (scanning electron microscope) imaging, which makes them extremely hard. As a part of my training with the machine, I obtained the images shown in figure 3.3: In figure 3.3 (a) the topography image of a fixed and dried liver cell and in figure 3.3 (b) the corresponding phase image is shown. The focus of interest was on the sub-micrometer pores which liver cells exhibit. In the phase image, the glass substrate shows as grey background with the cell darker on top. The best image quality was achieved in tapping mode, typical for this mode of operation is a phase below 90° as seen in the phase image. The phase image is capable of showing that the pores are indeed holes throughout the whole cell and that in fact the glass surface is imaged underneath. The goal was to be able to image the wet cells but the necessary equipment was not available at that time and therefore further analysis was not conducted.

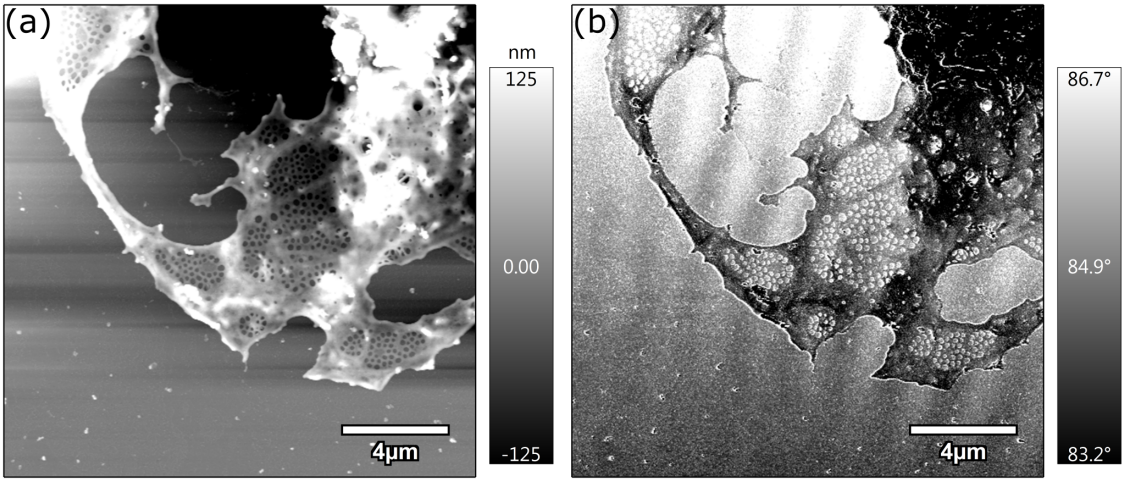

Figure 3.3: Dried and fixed liver cell treated with osmium tetroxide for SEM analysis on standard labortory glass sheet. (a) topography image (b) phase image

4 Hafnium Doped Zinc Oxides

The great abundance and low cost of ZnO make it especially interesting for the solar cell industry but despite showing promising results for different applications in this industry, the commercial applications are still pending. In the solar energy industry, it is crucial that production and material cost is kept as low as possible to be competitive with other cheap forms of electrical power supply like coal, hydro or wind power. In regions with high solar irradiance solar energy is already capable to compete and surpass the generation via fossil fuels [79] but a further decrease in cost could boost the solar energy market in other regions. In cooperation with members of the Khalifa University in Abu Dhabi, we conducted investigations of Hafnium doped ZnO (HZO or Hf-ZnO) to evaluate its potential to take over the role of ITO and reduce the indium demands for thin film solar cell production.

At room temperature ZnO has a hexagonal wurtzite structure with lattice parameter a = 3.25 Å and c = 5.21 Å, with a 1.6 c/a ratio. The hexagonal lattice type leads to favourable growth in c direction (typically perpendicular to the substrate) or perpendicular to it (typically parallel to the substrate) depending on the temperature [80]. Polycrystalline [81] and crystalline [82] ZnO thin films have been studied for optoelectronic applications. Due to its relatively large direct band gap around 3.3 eV, ZnO is transparent in the visible spectrum (1.6 - 3.1 eV) and is comparable to the band gap of ITO (3.5 - 4.3 eV) [83], whereas showing lower transparency in the ultraviolet regime due to the lower band gap. Many doping agents have been studied to modify the electrical, optical and structural properties of ZnO to achieve comparable results to ITO. Some doping materials like aluminium and magnesium

have been widely studied to tune the properties of ZnO for the specific applications e.g. for the use as TCO, aluminium (Al) doping has shown to enhance the optical and electrical properties [7, 84–86]. Furthermore, Al doping can be used to match the energy levels in inverted structure bulk heterojunction organic solar cells. In these cells, the ZnO layer is used as an electron transport layer (ETL), which is an extra layer in between the active layer and the front contact and takes the role of reducing recombination losses at the interface of those two. The Al doping leads to an upward shift in the ZnO Fermi level which enables the tunability of the energy level to reduce recombination losses at the interface [68–70]. In addition to enabling the tunability of the Fermi level, Al increases the optical band gap, making it more transparent for high energy photons, a desirable characteristic to increase the total conversion efficiency. Al doping increases the carrier concentration leading to higher electron conductivity, another desirable material property for electron transport layers as well as TCOs.

For some application such as an emitter in ZnO/Si heterostructure [87], magnesium (Mg) has shown more beneficial properties. Using textured ZnO/Si heterojunction Pietrysyka et al. [88] achieved an impressive conversion efficiency of 14%. They used a mixture of Al- and Mg-doped ZnO (MgZnO) to achieve this high conversion efficiency. Mg has some advantages as a doping agent due to its capability to enable a high tunability of the ZnO band structure by increasing the band gap up to 0.7 eV[89] and decreasing electron affinity by up to 0.46 eV[90]. The downside of MgZnO is an increased resistivity with increased doping concentrations compared to undoped ZnO [91–93]. A material with the high tunability of band structure like MgZnO without sacrificing high conductivity or even with an increase in conductivity is therefore desirable.

HZO is a potential candidate to achieve these qualities. HZO shows an increase in carrier concentration and a decrease in resistivity with doping concentration [94, 95]. Ahn et al. [94] and Geng et al. [95] reported a decrease in resistivity and enhancement in crystallinity up to doping concentration of 7%. Above 7%, a decrease in

conductivity and a degeneration of the crystallinity is observed, due to the formation of HfO_2 phases[94]. Consequently, the low doping regime is potentially interesting for the use as TCO and other solar cell applications.

4.1 Sample preparation

The Hf-ZnO thin films were grown on a silicon wafer by Atomic layer deposition (ALD) using an Oxford FlexAl ALD system and were provided by Boulos Alfakes (the samples preparation is described in more detail in [80]). ALD is a thin-film deposition technique similar to chemical vapour deposition (CVD) but using two or more gaseous species (referred to as precursors), which are alternated to grow the thin film but are never present in the reaction chamber at the same time. The reactions are self-limiting so that only one layer is grown each cycle. In our case three precursors were used, one for zinc oxide (ZnO), one for hafnium (Hf) and water vapour (H_2O) to create new reaction sites for the previous two. By varying the number of cycles for each precursor the doping concentration can be varied. Diethyl-zinc (DEZ) and water vapour are used to grow ZnO, while tetrakisethyl-methylaminohafnium (TEMAH) and water vapour are used for HfO_2. By varying the ratio of cycles of DEZ to TEMAH the doping was varied and by varying the total number of cycles a thickness of $\sim$75 nm was ensured. Deposition rates in the range of 0.083 to 0.196 nm per cycle were achieved, where higher values were measured for lower Hf doping. Prior to each deposition, the gas line was purged using 90 cycles of plasma HfO_2 on a dummy wafer. Growth temperature and pressure were 250 °C and 200 mTorr, respectively. The substrates were cleaned by solvent cleaning with rinses of acetone, isopropanol and deionised water and subsequently dried in a nitrogen atmosphere. Six samples with different doping concentrations were investigated and are referred to as the ZnO, 1:32, 1:9, 1:4, 1:1 and 2:1 sample according to the ratio of DEZ and TEMAH cycles. Since small doses of the TEMAH

precursors were used, even the 2:1 sample should show doping concentrations of Hf lying in the low percent regime, but a quantitative analysis is still pending.
Pressurised nitrogen was used to blow possible dust off the sample, otherwise, no further sample preparations were necessary for the investigation with the AFM. The samples were exposed to ambient air for several weeks before the first measurements were conducted and can, therefore, be considered in a "stable" condition, meaning that no further surface ageing or formation of water layers is assumed during the measurement cycles.

4.2 Measurements

X-ray diffraction (XRD), TEM, optical and electrical measurement were carried out by members of the Department of Materials Science and Engineering and the Department of Microsystems Engineering of Khalifa University in Abu Dhabi and are presented here for completeness and to underline the results of our investigations. The AFM measurements were conducted by me with support of Chia-Yun Lai.

Force Curves

Force curves were obtained by measuring amplitude and phase versus distance (APD) curves and reconstructing the force via the Sader-Jarvis-Katan[30, 33] formalism (sec 2.1.6). To determine the position where the APD curves were taken the samples were scanned prior to each set consisting of approximately 100 curves. The samples were left in the sample holder for several hours to avoid/reduce thermal drift since a location-specific measurement would not have been possible otherwise. Still, it was not always possible to record 100 APD curves at one spot due to thermal drift. The signal was monitored all the time and if strong changes occurred the measurement was stopped and the APD curves discarded. The minimum critical amplitude was determined for several spots to retrieve a range for the minimum

critical amplitude on the sample and, subsequently, A_{Cm} was approximated by the centre of this range. A precise measurement of critical amplitude is not mandatory to reconstruct the force, but would be essential to accurately monitor the tip radius. The free amplitude was set accordingly to $A_1 > 3A_{\mathrm{Cm}}$ or higher, typically $A_1 \approx 90 - 140\,\mathrm{nm}$, to ensure a smooth transition from the attractive to repulsive regime (sec. 2.1.7).

A reduction from initial $\phi_1 = 90°$ to $\phi_1 \approx 82°$ at d_{min} is sufficient to reconstruct the force and a further approach enhances the risk of tip degradation. Consequently, the trigger point for retracting was set as high as possible and continuously adjusted to still achieve a reduction to $\phi_1 \approx 82°$. Thermal calibration [45] was carried out approximately 50 nm above the sample surface. Several unsuccessful attempts were made to measure Hamaker constants reliably throughout the different samples and were ultimately replaced by the bimodal imaging method to measure Hamaker constants. The difficulties caused by the high heterogeneity and thermal drift could not be overcome and made the force curves an unreliable tool to compare the different samples. Standard AC240TS - R3 OLYMPUS cantilevers with radius $R_{\mathrm{tip}} \approx 7\,\mathrm{nm}$, stiffness $k_1 \approx 2\,\mathrm{N/m}$, Q factor $Q_1 \approx 120$ and resonance frequency $f_1 \approx 80\,\mathrm{kHz}$ for the first mode were used to conduct the experiments.

Bimodal Imaging

In order to acquire bimodal images of the differently doped Hf-ZnO samples, the first and second mode of the cantilever were excited at their respective resonance frequency. The main advantage of bimodal imaging is the additional information that can be obtained with the two additional channels (amplitude and phase) of the second mode. This information was used to retrieve Hamaker maps of each sample, which can be averaged to obtain a comparable value if done correctly [63]. Since the goal was to be able to achieve results that allow for comparison throughout the samples, the critical amplitude A_{Cm} had to be measured on each sample and provided the crucial information to set the free amplitudes of the first and second

mode. This has proven to be more challenging than expected since the samples show high heterogeneity in sample properties. This heterogeneity leads to variations in the measured minimum critical amplitude of up to 10 nm depending on the location of the sample, while typical values for $A_{\mathrm{Cm}} \approx 15 - 25\mathrm{nm}$. This behaviour led to difficulties especially in the beginning when it was not yet clear, what was causing the inconsistent behaviour in critical amplitude. Thermal drift led to the impression that the minimum critical amplitude was changing over time, while in reality, the sample surface is moving due to thermal expansion (thermal drift), changing the tip location on the surface over time. To overcome these difficulties in accurately measuring the minimum critical amplitude, the samples were scanned and several spots picked to measure the minimum critical amplitude. Subsequently, the different values were roughly approximated and used to set the free amplitude of the first mode A_{01} to $A_{01}/A_{\mathrm{Cm}} \approx 0.5$. This procedure was repeated for all the samples, to keep this ratio constant on each sample. The importance of this ratio to achieve comparable results was highlighted in [63], although our aim was not to achieve quantitative results, it is crucial to have the same A_{01}/A_{Cm} value on each sample to be able to compare the results of the samples to each other. A_{02} was set to approximately 3% of A_{01}, typical amplitude values for these samples are $A_{01} \approx 10\,\mathrm{nm}$ and $A_{02} \approx 0.3\,\mathrm{nm}$. Due to a high amplitude response of the cantilever to the excitation of the second mode and a lack of fine-tunability of the excitation amplitude at low values, A_{02} could not always be set to 3% of A_{01}, but variations have been accounted for in the calculations. The amplitude of the first mode A_1 was used as a feedback signal and set to $A_{\mathrm{SP}} = 0.8 \cdot A_{01}$ for bimodal imaging in the attractive regime and for bimodal SASS to approximately $A_{\mathrm{SP}} \approx 1\,\mathrm{nm}$. Since a very low error signal of a few Å was achieved, $A_{\mathrm{SP}} = A_1$ is assumed further on. The data presented were collected by two different AFM users using different tips and the order of the samples was changed for the measurement cycles, to ensure that the trend is not replicated by some sort of tip degradation throughout the measurements. Unfortunately, due to contamination on one of the samples, the tip had to be changed during one measurement cycle.

Standard OLYMPUS cantilevers (AC240TS - R3) with radius $R_{\text{tip}} \approx 7\,\text{nm}$, stiffness $k_1 \approx 2\,\text{N/m}$ and $k_2 \approx 75\,\text{N/m}$, Q factor $Q_1 \approx 120$ and $Q_2 \approx 400$, resonance frequency $f_1 \approx 80\,\text{kHz}$ and $f_2 \approx 450\,\text{kHz}$ for the first and second mode respectively were used to conduct the experiment. The calibration of the first and second mode was determined by thermal analysis near the surface ($\sim$50 nm) and repeated for each sample.

4.3 Results and Discussion

TEM and XRD analyses show that at an elevated growth temperature of 250 °C mostly substitution of Zn with Hf atoms occurs. XRD results indicate lattice parameters $a = 3.24\,\text{Å}$ and $c = 5.2\,\text{Å}$ with no significant variation throughout all the samples. TEM analysis (fig. 4.1) of the cross section of the sample showed a thickness of 85 nm in contrast to ellipsometry analysis suggesting a thickness of 75 nm [80].

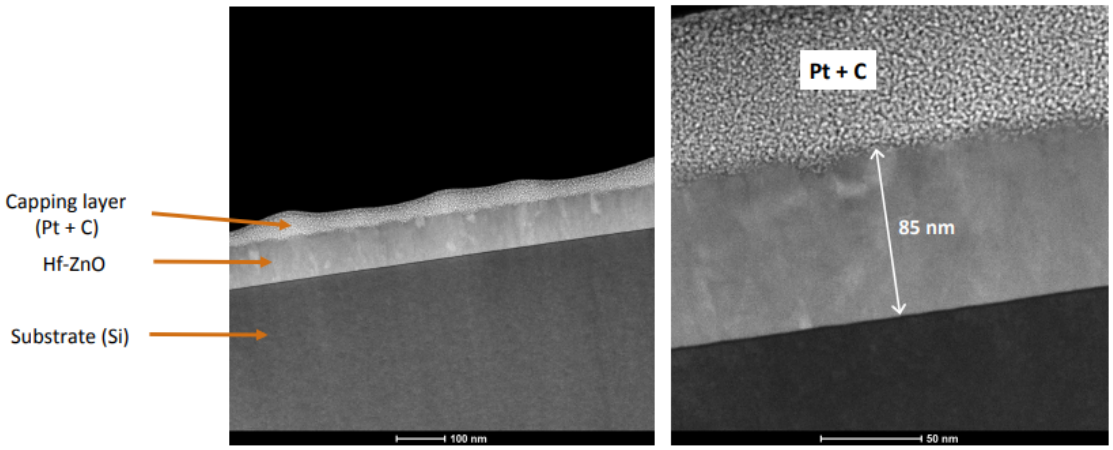

Figure 4.1: TEM image of the cross section of the 1:1 sample. The platinum carbon (Pt+C) capping layer was added during sample preparation for the TEM imaging

The HRTEM (high-resolution transmission electron microscopy) images and espe-

cially the fast Fast Fourier Transform (FFT) of the image indicate that the samples are polycrystalline as seen in figure 4.2. Furthermore, the TEM investigations show no visible amorphous regions, cracks or pores in the sample. The images show a section of the cross section with the same orientation as figure 4.1.

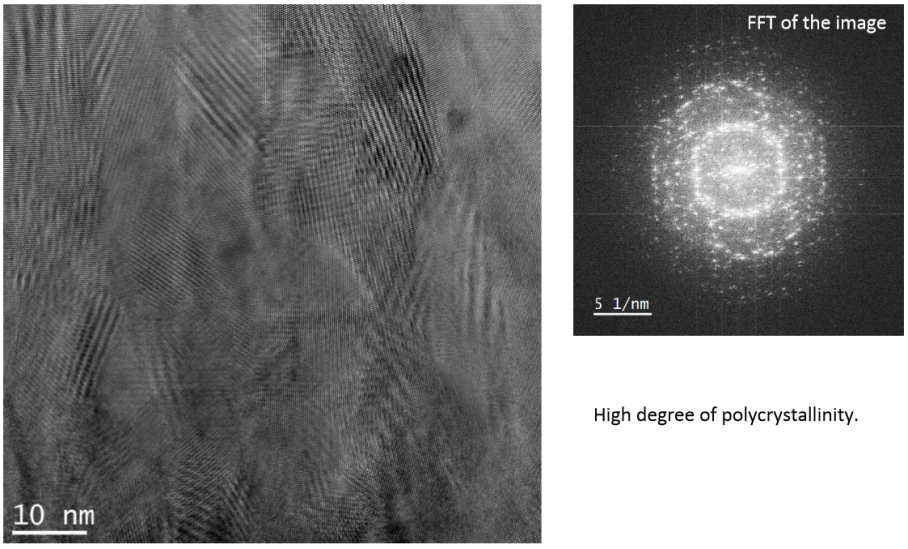

Figure 4.2: HRTEM analysis of the 1:1 sample show polycrystallinity of sample. Left: HRTEM image of the cross section. Right: fast Fourier transform of the image

The elemental distribution was investigated via energy-filtered TEM (EFTEM). The images (fig. 4.3) indicate a homogeneous distribution of Zn and O throughout the film. On top, the carbon and platinum in the capping layer is visible which was added during sample preparation for TEM imaging, while underneath the silicon (Si) of the Si wafer used as substrate is visible. The Hf doping concentrations are too low to be visible due to core losses, this suggests that the 1:1 sample doping concentration is lower than 7% since Ahn et al. [94] observed short ranging HfO_2 above 7% doping concentrations, which would most likely be visible in the EFTEM image.

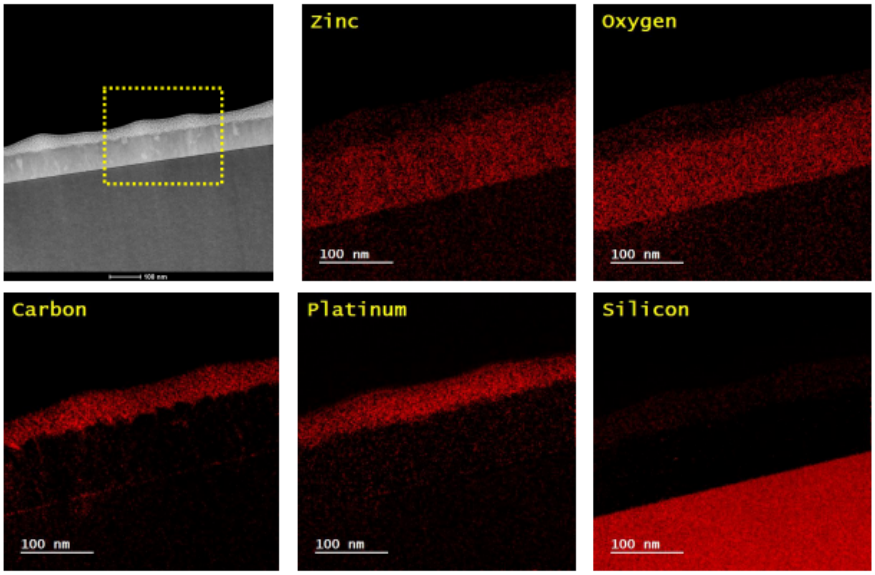

Figure 4.3: EFTEM images showing the elemental distribution throughout the cross section of a HZO film with cycle ratio 1:1.

4.3.1 AFM - Bimodal imaging

Topographical images

500 nm-overview images of all the sample were taken to show the topography of the samples (fig. 4.5). The images shows a typical feature size of several tens of nanometer[96, 97] with height variations/roughness of a few nanometers (table 4.1). The AFM images show a spike-like shape for ZnO transitioning to a more round shape for higher doping concentration that has been observed in SEM images (fig.4.4 and [96, 97]).

The AFM and SEM image of Zno (fig. 4.4 and 4.5) show similar shapes but the AFM is not able to reproduce the SEM images exactly. The AFM images show more round round shapes than the SEM image this might be partly due to the limiting of resolution of topographical features with approximately the same size as the tip as illustrated in 4.6. Note that the illustration simplifies the situation, since in reality the tip did not achieve mechanical contact during recording of the images.

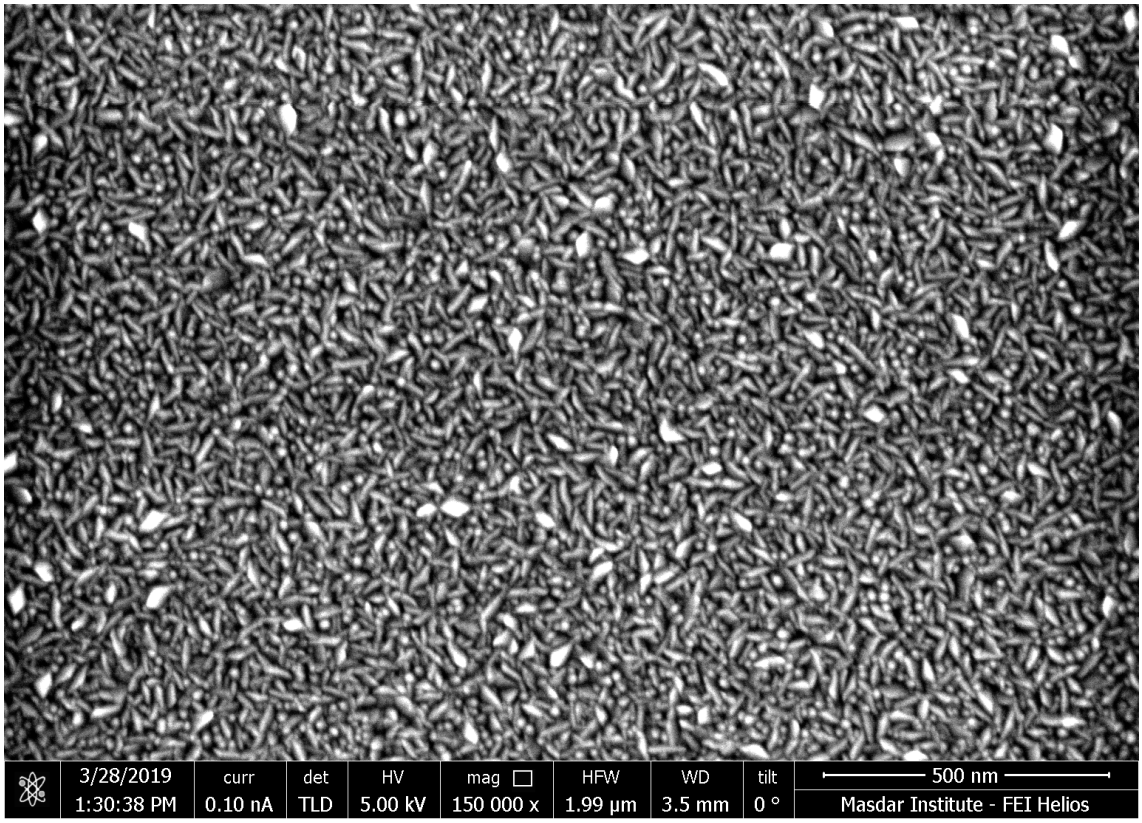

Figure 4.4: SEM image of the ZnO sample showing spike like shapes.

This limitation is most likely contributing to the different appearance of the SEM and the AFM image but other factors might contribute. The difference in observed images could be caused by different sensitivities to sample properties of the used methods. The height image of the AFM is only sensitive to topography whereas the SEM is sensitive to topography but also other morphological variations like crystal orientation.

Table 4.1: Roughness for the six samples calculated by the build in function of *Asylum Research*

Sample	ZnO	1:32	1:9	1:4	1:1	2:1
Roughness (SD)/nm	3.229	2.594	2.357	2.658	2.511	3.530

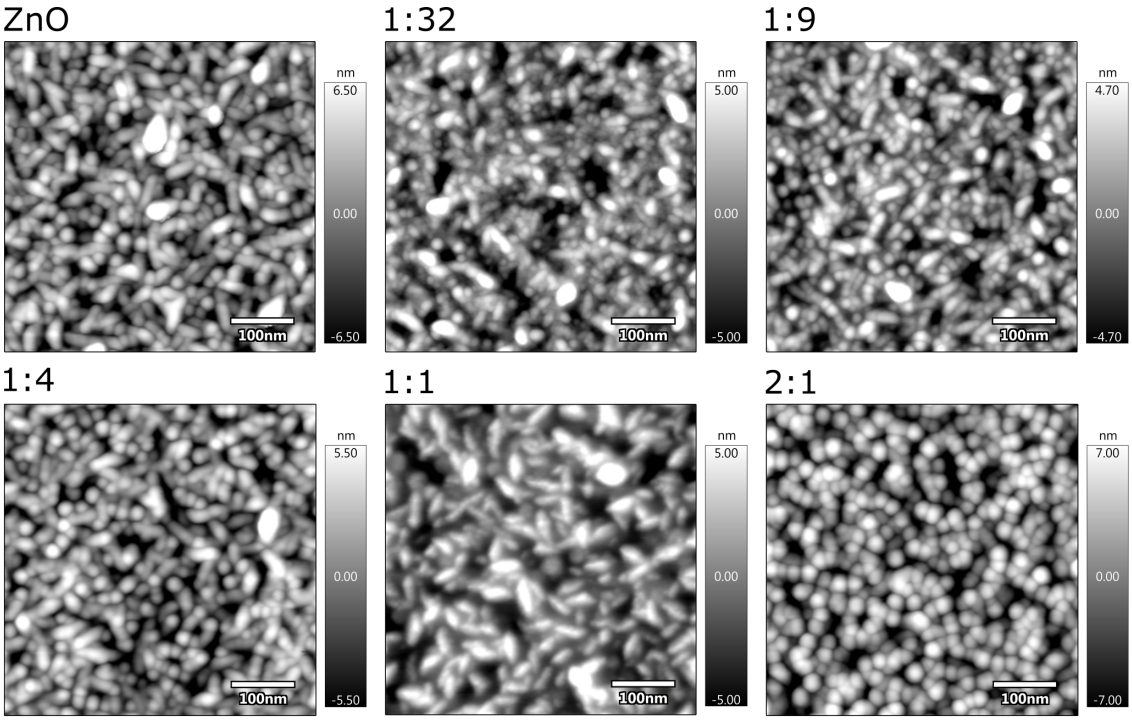

Figure 4.5: Topographic AFM-images of the differently doped Hf-ZnO samples. Showing the transition from spike shapes to more round shapes with increasing doping concentrations.

Phase image

The obtained phase images show phase contrast in the first (fig. 4.7 (c)) as well as in the second mode (fig. 4.7 (d)) for all samples, that does not seem to be related to a bad integral gain of the feedback signal (sec. 2.1.5). To avoid a misinterpretation the integral gain was carefully set to achieve variations in the amplitude signal of the first mode in the low Å region (fig. 4.7 (b)). Due to the low variations in A_1, it is a reasonable assumption that the contrast seen in figure 4.7 (c) and (d) is real. On several samples, darker edges were observed to appear always on the same side of the feature. To ensure that these darker edges are not due to any "parachuting off"-effects, the same images were taken with different scanning angles. Phase contrast due to the "parachuting off" of features should not turn with the image since the tip is always moving horizontally across the imaged area. Since the darker edges turn with the sample image as the scan angle is changed (fig. 4.8), it is assumed that

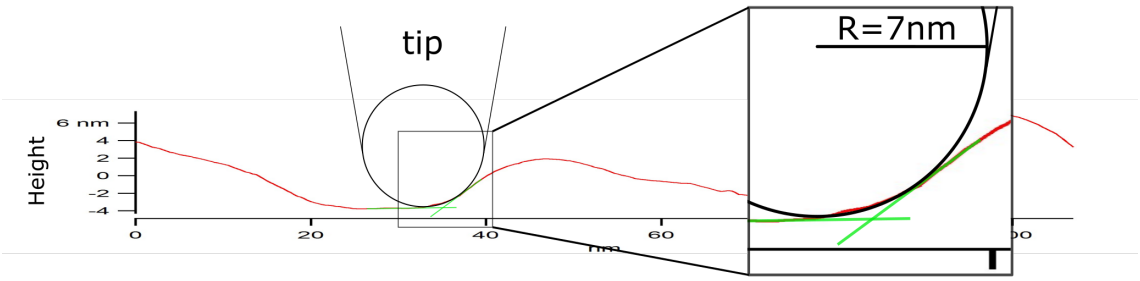

Figure 4.6: Height profile along a line on the ZnO sample and a schematic drawing of the tip scanning the surface. Edges of the sample will appear more round in the images than they truly are due to the small feature size with roughly the same size as the tip (radius ∼7 nm).

phase contrast is not caused by problems associated with badly set integral gain or too fast scan rates. The fact that the features seem to show phase contrast on the same side, indicates a favourable growth direction towards one side, possibly caused by directional gas flow or other asymmetries during the growth process of the thin film. We are not fully confident what leads to the phase contrast on the samples but it could be explained by different crystal planes being probed. The crystal planes show variations in the phase image due to different Young's moduli [98] or different surface propertiesaccording to orientation [99].

Force curves and bimodal imaging

We recorded APD curves and reconstructed the forces as described in section 2.1.6 for the 2:1 sample (fig. 4.9). Two types of regions were distinguished in the ϕ_1 image (black and grey see figure 4.9 (b)) with 300 curves taken on each region. To ensure that the APD curves could be recorded at the intended position, the sample was left in the sample holder overnight to thermally stabilise. Hundred curves were recorded in succession before the sample was scanned again to ensure a correct tip positioning. The curves show different behaviour in the attractive as well as in the repulsive regime. This highlights the problems of using force curves on these HZO samples to achieve comparable results between the samples. If force curves are

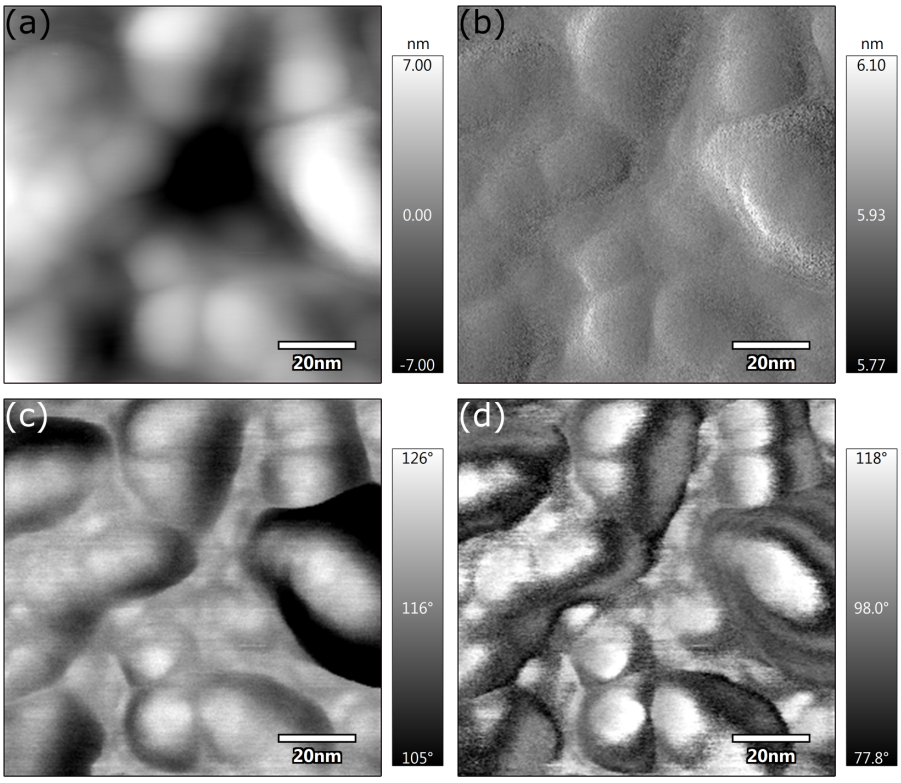

Figure 4.7: Height (a), Amplitude of first mode/error signal (b), phase of first mode (c) and phase of second mode (d) of ZnO with scan size of 100 nm

recorded on each sample, differences might be due to variations within each sample and might falsely be interpreted as differences due to doping concentrations.

Further analysis have shown that it is not a binary transition from the force profile achieved on the grey region to the one achieved in the black region, everything in between is also possible. It is not clear what causes the differences but a possible explanation is the probing of different crystallographic planes due to different crystal orientations. TEM investigations confirms the polycrystallinity of the samples, so variations in orientation are likely to occur.

To evaluate the reliability of the bimodal imaging method to retrieve Hamaker constants instead of force curves, force curves and a bimodal image were taken on the same sample with the same tip, the results are shown in figure 4.10 and discussed below.

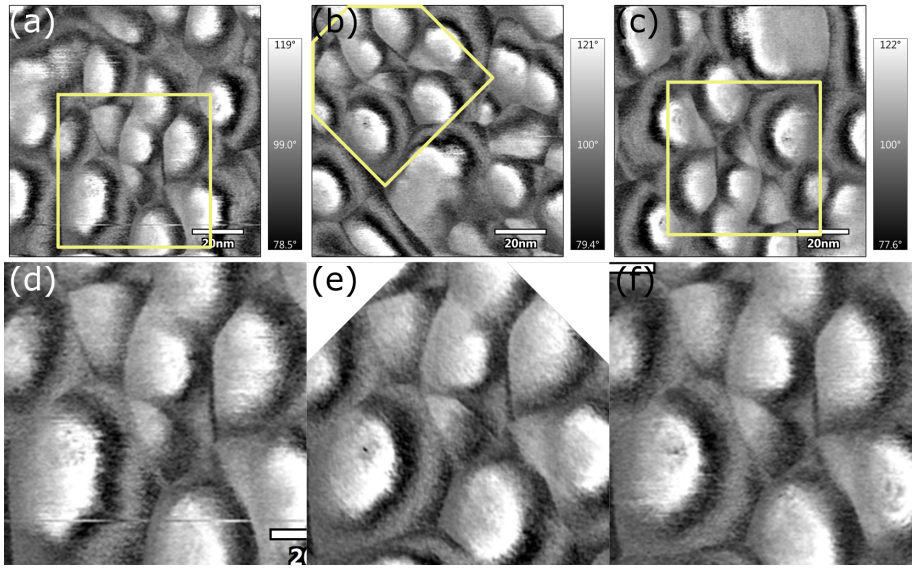

Figure 4.8: Second phase ϕ_2-image with (a) 0°, (b) 45° and (c) 180° scan angle and (d),(e) and (f) the according turned and cropped images of the same sample section

Bimodal imaging

Due to the high heterogeneity, force curves are not a reliable tool to measure the Hamaker constant. To achieve trustworthy results many different positions on the sample would need to be taken into account and these positions would need be representative for the sample. It is crucial that tip degradation is avoided to achieve comparable results throughout the samples and the parameters have to be fine-tuned from time to time, making an automated process of taking force curves on the sample difficult. Due to the combination of thermal drift, high heterogeneity and the risk of tip degradation during measurement, recording APD curves is a tedious work even on a single sample. In conclusion, our methods to record APD curves and reconstruct the force distance curves are not a reliable tool to measure Hamaker constants representative for the whole sample. Therefore, they should not be used to compare Hamaker constants among the different HZO samples.

A statistically more reliable approach is the use of bimodal imaging and retrieving the Hamaker constant for each point by the methods described in section 2.1.9. The correct averaging over the different sample areas is intrinsic in this method, since

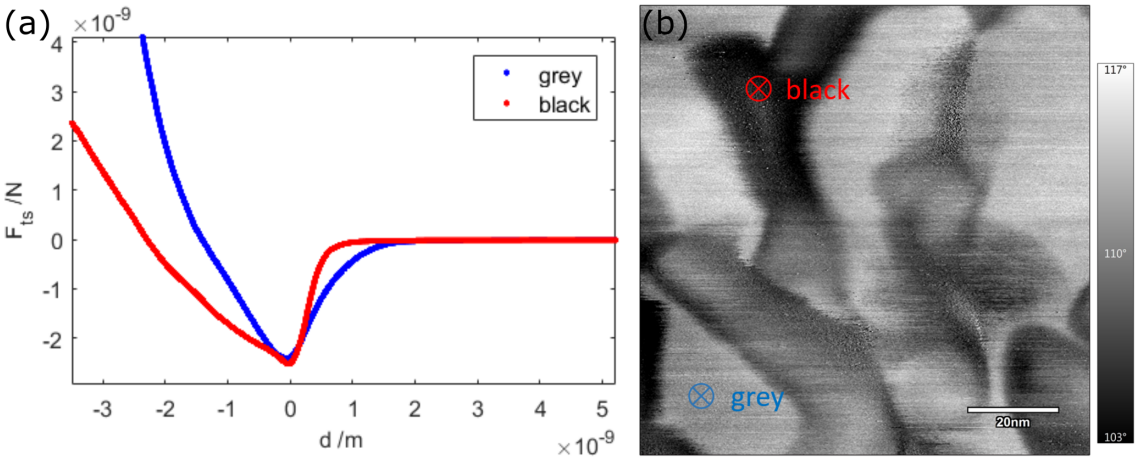

Figure 4.9: (a) reconstructed force curves and (b) positions on 2:1 sample

every pixel ($256 \cdot 256 = 65536$) gives one value for the Hamaker constant for the specific spot. The measurement itself and the data processing is more complex but holds the advantage of statistical more reliable results [63].

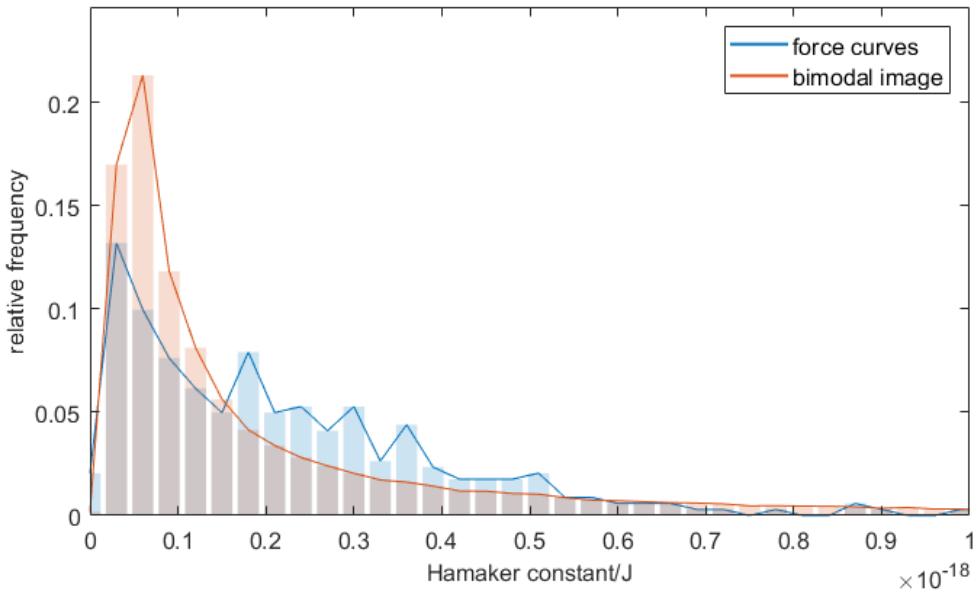

Figure 4.10: Hamaker constant distribution taken on the ZnO sample via force curves (red) and bimodal imaging method (blue).

To ensure that the not wildly used method of retrieving Hamaker constant via bimodal imging achieves reliable results on the HZO samples, the methods are compared to each other. One sample was scanned in bimodal imaging with APD

curves recorded subsequently as described in the previous section. Histograms of the Hamaker constants retrieved via forces curves and via bimodal imaging are shown in figure 4.10. It is not expected that the histograms show the same peak, since the force curves have the problem of not being statistical representative as previously discussed but the results should be similar. Assuming that the distribution of Hamaker constants retrieved via bimodal imaging is the real Hamaker constant distribution, then the Hamaker constants retrieved via APD curves should lie somewhere within the distribution retrieved via bimodal imaging. The results indicate that our method of retrieving Hamaker constants through bimodal imaging is comparable to the method of retrieving it via APD curves. Furthermore, it can be noted that the distribution achieved by the bimodal method has a single peak with a long tail towards higher Hamaker constants. To clarify the problem with the reconstructed force curves: one or several of the spots chosen to record APD curves, could be a spot with the very high Hamaker constant we see in the tail of the distribution. In that case the retrieved average Hamaker constant might appear substantially larger then the values achieved with bimodal imaging.
We believe that the distribution of Hamaker is not caused by measurement uncertainties but is caused by real variations in Hamaker over the sample, but our interest lies mainly in the average Hamaker constant since it represents the average surface interaction and in most other methods only average Hamaker constants are retrieved. Therefore, the distribution is not more closely investigated but it is noted that the distribution might be interesting for other application like the use of zinc oxides as photocatalyst [100, 101].

Effect of doping concentration on material properties

Bimodal images were obtained to measure the variations of the Hamaker constant with different Hf doping concentrations. Since the measuring procedure is time-consuming and difficult, only 3 sets of measurements were conducted. While two

measurements were performed consecutively with slight variations in setpoint, the third measurement was performed by a different AFM user and only included the ZnO, 1:9, 1:1 and 2:1 sample to confirm the trend.

Hamaker maps of all samples are shown in figure 4.11. An increase in areas with larger Hamaker constants can be observed up to a drastic change for the 1:1 sample while the 2:1 sample looks similar to the ZnO, 1:32 and 1:9 samples. The 1:4 sample already exhibits a significantly larger average Hamaker constant. The histograms of the retrieved Hamaker constants are plotted in figure 4.12, with the averaged and normalised Hamaker constants for the measurement series are shown in figure 4.13. The method used to retrieve Hamaker constants does not provide an error estimate for the retrieved values and the variations in results are believed to be mainly caused by the inaccurate measurement of critical amplitude. Further measurements are needed to determine the error of the applied method and, consequently, no error bars are given.

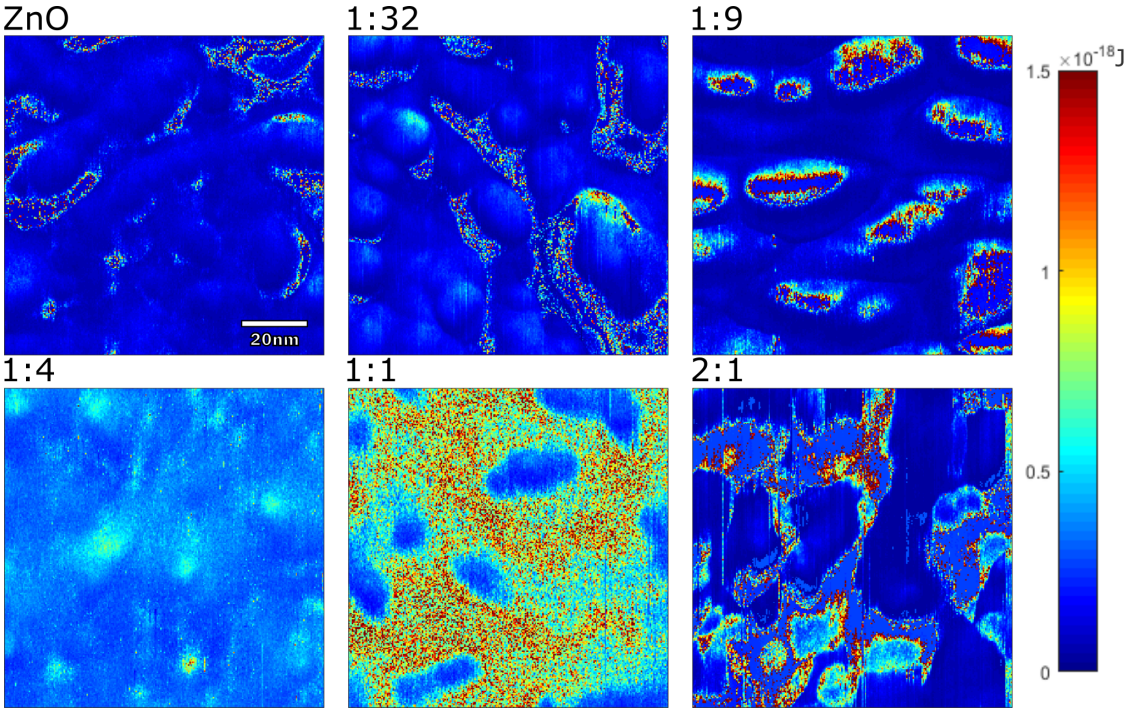

Figure 4.11: Hamaker maps retrieved from bimodal imaging of the six differently doped Hf-ZnO samples

We are not interested in the quantitative value of the Hamaker constant but its

trend depending on doping concentrations, therefore the values were normalised to the value of the ZnO sample. The maximum Hamaker constant lies within the range of the 1:4 and 2:1 sample. Further investigation with smaller steps in cycle ratio should be conducted to determine the cycle ratio, where the curve peaks more precisely.

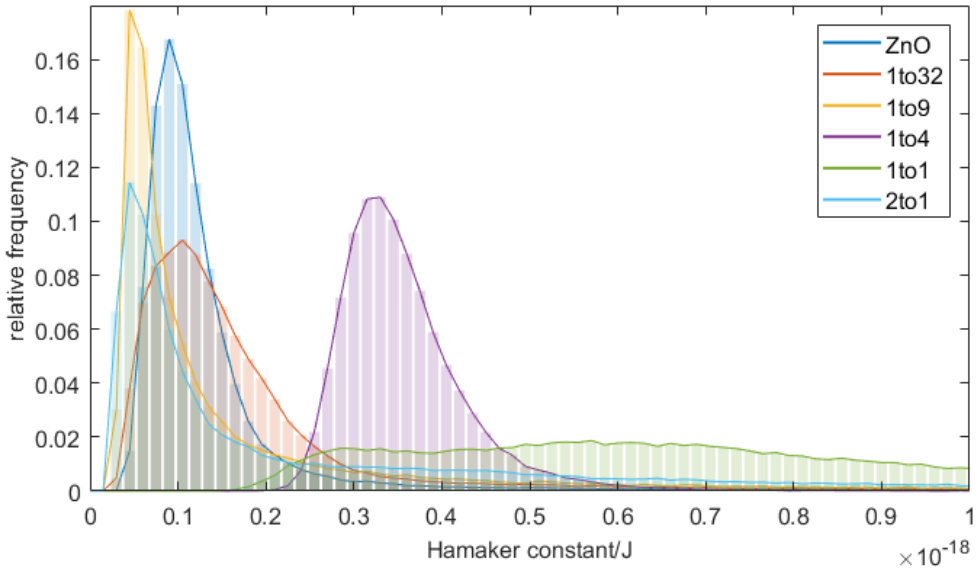

Figure 4.12: Histogram of Hamaker constants retrieved via bimodal imaging on all six differently doped Hf-ZnO samples

Hamaker constant and force of adhesion are directly linked by equation 2.5. To confirm our results we conducted bimodal SASS measurements and used them to create F_{AD}-maps of the ZnO, 1:9, 1:1 and 2:1 sample seen in figure 4.14 (a). The average force of adhesion (fig. 4.14 (b)) confirms the trend that is observed for the Hamaker constant.

The band gap (fig. 4.15 (a)) exhibits the same trend as the Hamaker constant of increasing with doping concentration until it reaches a maximum for the 1:1 sample before decreasing for the 2:1 sample. The increase in band gap can be attributed to the Burstein-Moss effect [102, 103], the higher doping causes the filling of the lowest states in the conduction band, shifting the Fermi level above the conduction band minimum, the semiconductor is then referred to as degenerated. The larger

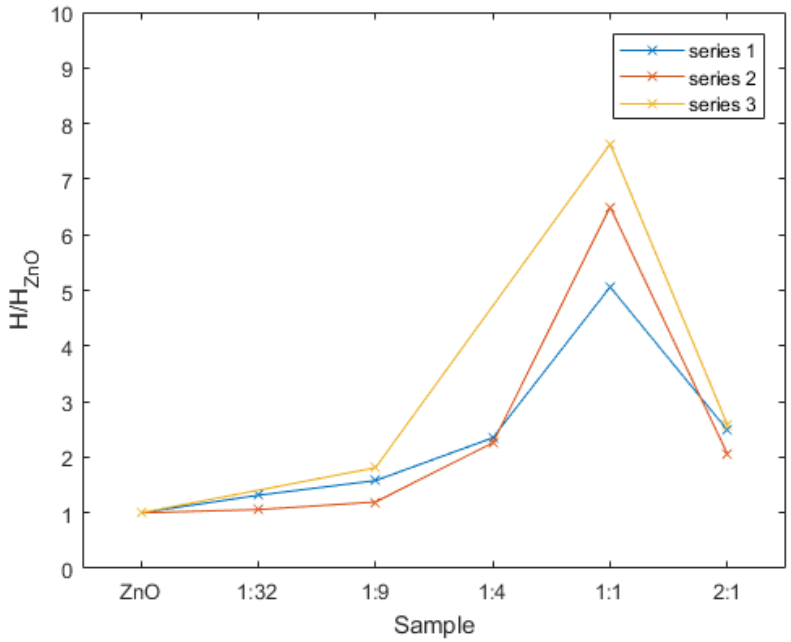

Figure 4.13: Hamaker constants in dependence of varying cycle ratio. Series 1 and 2 were taken subsequently and included all six samples, while series 3 only inlcludes the ZnO, 1:9, 1:1 and 2:1 sample.

band gap allows more energetic photons to be transmitted and reach the substrate underneath. The substrate could be the active layer in a solar cell, if the HZO is used as TCO, ETL or emitter. First principle DFT calculations have shown an increase in band gap with increasing Hf concentrations and a substitution of Zn by Hf in the wurzite structure which agrees well with the experimental results [80]. Furthermore, an increase of transmittance in the visible and near-infrared region can be observed for the samples up to the 1:4 cycle ratio (fig. 4.15 (b)). A high transmittance is essential for the use as TCO in solar cells. For the 1:1 and 2:1 sample a shift of the transmission curve towards shorter wavelengths can be observed. Depending on the application, the shift might be desirable or a lower doping concentration, where no shift is observed could fit the application better and has to be analysed for the specific application.

Higher doping concentrations lead to a higher charge carrier concentration η, which is typical for higher substitutional doping concentrations. Simply speaking, every Hf

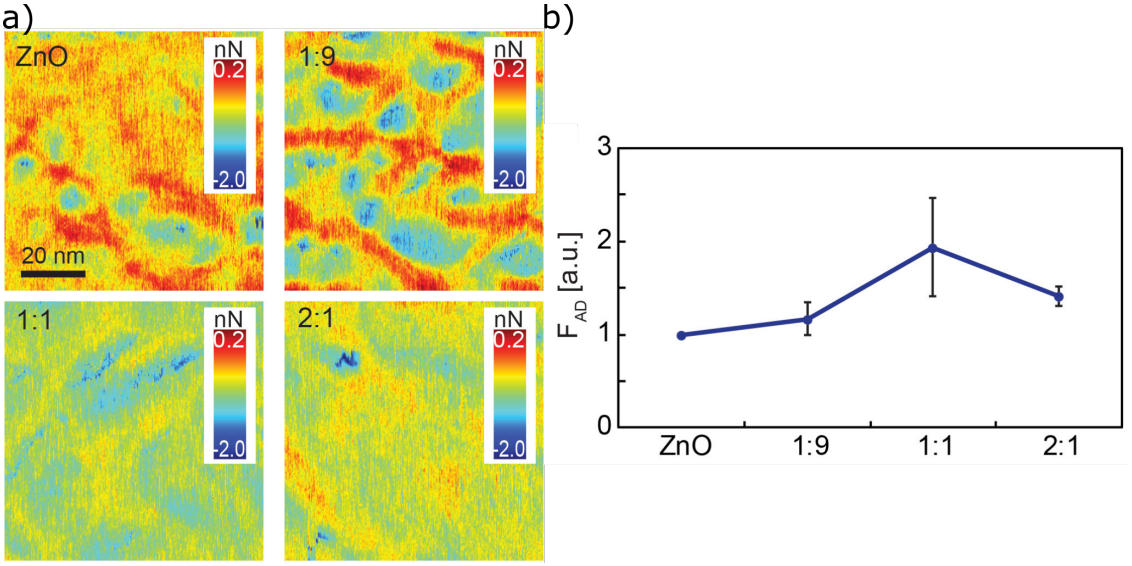

Figure 4.14: Force of adhesion retrieved via bimodal SASS for the ZnO, 1:9, 1:1 and 2:1 sample. (a) Force of adhesion maps, (b) averaged force of adhesion normalised to the undoped ZnO sample

atom contributes two free electrons to the system since it has four valence electrons and Zn only has two. At higher doping concentrations short-range HFO_2 phases form that do not contribute to the increase of η. The charge carrier mobility ν is decreased due to the higher number of defects that higher doping concentrations are accompanied with. The resistivity ρ is inverse proportional to $\nu \cdot \eta$. Since ν decreases to roughly half its value but η increases six-fold, ρ decreases by over a factor of 3 from 6.1 mΩ cm for undoped ZnO to 1.6 mΩ cm for the 1:1 sample. A low resistivity/high conductivity is essential for the application as TCO and desirable in most other applications in solar cells. The decrease of η and consequently increase of ρ has been linked to the formation of short-range HfO_2 phases [94].

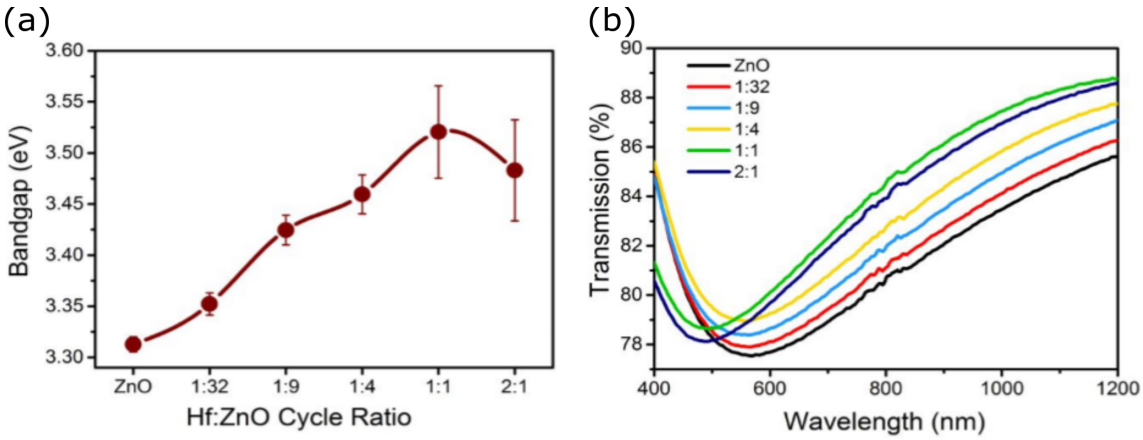

Figure 4.15: Optical properties for the six different samples. (a) band gap extracet via tauc plots and fitting, (b) trnassmision of HZO films deposited on a quarz substrate(without correction for the substrate). Graphs thankfully received from [80]

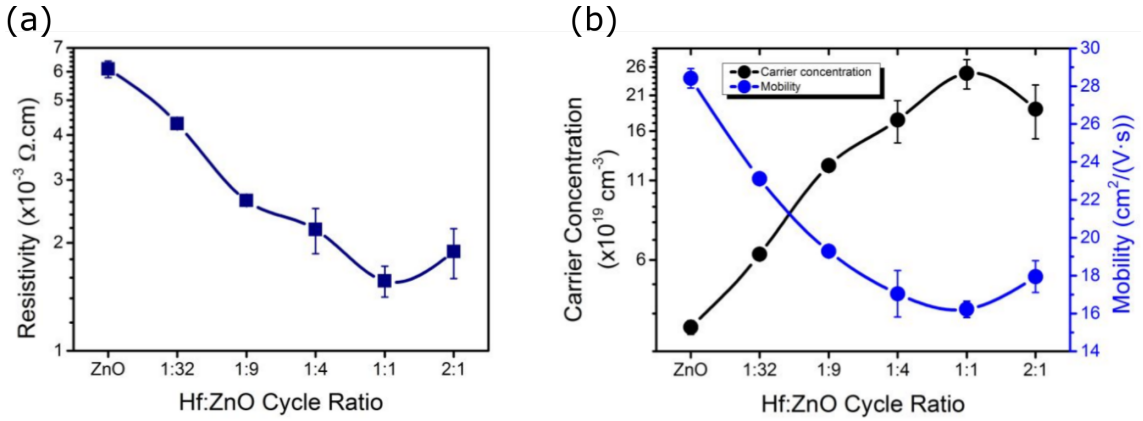

Figure 4.16: Electrical properties from Hall Effect measurements for the six different samples. (a) resistivity and (b) carrier concentration and mobility. Graphs thankfully received from [80]

5 Conclusion

Hamaker constant measurements were conducted via bimodal imaging method and compared to measurements via reconstructed force curves. Hamaker constants retrieved via force curves have shown to be strongly dependent on the position on the sample, but in general agree with the distribution retrieved via bimodal imaging. Force curves are not considered to achieve representative results on HZO samples due to the high heterogeneity. We suggest this high heterogeneity is due to different crystallographic planes showing different surface properties. Different crystallographic planes being probed can be linked to the polycrystallinity of the samples which was confirmed by HRTEM.

The change from a spike-like feature shape to a more round one with increasing doping concentrations, as seen in SEM images in previous studies [94, 95], could be confirmed with the AFM. We were able to show that the average Hamaker constant increase with increasing doping concentration until a peak is reached at a 1:1 cycle ratio, after that a sharp drop is observed. The bimodal SASS imaging method was used to retrieve the average force of adhesion for the samples. The direct relation between the force of adhesion and Hamaker constant allowed us to confirm the trend in Hamaker constant.

Optical and electrical measurement have shown the same trend for the band gap and carrier concentration. Consequently, doping concentrations up to the 1:1 cycle ratio, are especially interesting for the use as front contact or electron transport layer in solar cells. Optical measurements have shown an increase in transmittance in the visible and near infrared up to the 1:4 cycle ratio and a shift for higher concentra-

tions. A more reliable method to measure the critical amplitude on these samples could lead to quantitatively trustworthy results of Hamaker constants measurements. Quantification of the doping concentration is still pending and will provide insights if our results agree with the result of other studies [94, 95]. Finally, smaller steps in doping concentrations should be realised to determine the exact peak position.

6 Acknowledgement

I want to thank Matteo Chiesa for supervising my work in Tromsø and providing me with the opportunity to do my master thesis in this field. I especially want to highlight the friendliness and hospitality with which he welcomed me into the group. There was always the opportunity to talk about non-university-related topics, creating a pleasant atmosphere to work in. I also want thank Chia-Yun Lai for introducing me to the machine and teaching me everything I know about AFM operation. Without her help and expertise in the field, this work would have not been possible. The informal working atmosphere was really pleasant and it was a welcome distraction to be able to joke around and that not only work-related topics could be discussed.

Furthermore, I want to thank Paul Scheier for the uncomplicated supervision in Innsbruck, Boulos Alfakes for providing the samples and his results, Nitul Rajput for his TEM and SEM analysis and Arne Schiller for proofreading my thesis.

Finally, I want to thank my family who supported me in doing this thesis abroad and always trust me in my judgment of career path.

Bibliography

[1] C. Figueres, C. Le Quéré, A. Mahindra, O. Bäte, G. Whiteman, G. Peters, and D. Guan. Emissions are still rising: ramp up the cuts. *Nature*, 564 (7734):27–30, December 2018. doi: 10.1038/d41586-018-07585-6. URL https://doi.org/10.1038/d41586-018-07585-6.

[2] M. Lokanc, R. Eggert, and M. Redlinger. The availability of indium: The present, medium term, and long term. Technical report, oct 2015. URL https://doi.org/10.2172/1327212.

[3] B. Stannowski, F. Ruske, S. Neubert, S. Schönau, S. Ring, S. Calnan, M. Wimmer, O. Gabriel, B. Szyszka, B. Rech, and R. Schlatmann. Potential of high-mobility sputtered zinc oxide as front contact for high efficiency thin film silicon solar cells. *Thin Solid Films*, 555:138–142, March 2014. doi: 10.1016/j.tsf.2013.10.014. URL https://doi.org/10.1016/j.tsf.2013.10.014.

[4] C. Hsiung Lin, K. Hsiang Chuang, S. Hsien Lin, C. Hsiung Chang, K. Chih Lin, and C. Yao Tsai. Commercial large area bi-layered zinc oxide as front contact in tandem silicon thin film solar cell. In *2011 37th IEEE Photovoltaic Specialists Conference*. IEEE, June 2011. doi: 10.1109/pvsc.2011.6186473. URL https://doi.org/10.1109/pvsc.2011.6186473.

[5] J. A.A. Selvan, H. Keppner, U. Kroll, J. Cuperus, T. Adatte, C. Ketterer, and A. Shah. Material aspects of zno to make surface texture growth for light trapping for thin film solar cells. *Helvetica Physica Acta*, 70:9–10, 1997.

[6] O. Kluth, B. Rech, L. Houben, S. Wieder, G. Schöpe, C. Beneking, H. Wagner, A. Löffl, and H.W. Schock. Texture etched ZnO:al coated glass substrates for silicon based thin film solar cells. *Thin Solid Films*, 351(1-2):247–253, August 1999. doi: 10.1016/s0040-6090(99)00085-1. URL https://doi.org/10.1016/s0040-6090(99)00085-1.

[7] J. Müller, B. Rech, J. Springer, and M. Vanecek. TCO and light trapping in silicon thin film solar cells. *Solar Energy*, 77(6):917–930, December 2004. doi: 10.1016/j.solener.2004.03.015. URL https://doi.org/10.1016/j.solener.2004.03.015.

[8] M. Berginski, J. Hüpkes, M. Schulte, G. Schöpe, H. Stiebig, B. Rech, and M. Wuttig. The effect of front ZnO:al surface texture and optical transparency on efficient light trapping in silicon thin-film solar cells. *Journal of Applied*

Physics, 101(7):074903, April 2007. doi: 10.1063/1.2715554. URL https://doi.org/10.1063/1.2715554.

[9] S. Faÿ, L. Feitknecht, R. Schlüchter, U. Kroll, E. Vallat-Sauvain, and A. Shah. Rough ZnO layers by LP-CVD process and their effect in improving performances of amorphous and microcrystalline silicon solar cells. *Solar Energy Materials and Solar Cells*, 90(18-19):2960–2967, November 2006. doi: 10.1016/j.solmat.2006.06.003. URL https://doi.org/10.1016/j.solmat.2006.06.003.

[10] L. Ding, M. Boccard, G. Bugnon, M. Benkhaira, S. Nicolay, M. Despeisse, F. Meillaud, and C. Ballif. Highly transparent ZnO bilayers by LP-MOCVD as front electrodes for thin-film micromorph silicon solar cells. *Solar Energy Materials and Solar Cells*, 98:331–336, March 2012. doi: 10.1016/j.solmat.2011.11.033. URL https://doi.org/10.1016/j.solmat.2011.11.033.

[11] B. Hussain, A. Ebong, and I. Ferguson. Zinc oxide as an active n-layer and antireflection coating for silicon based heterojunction solar cell. *Solar Energy Materials and Solar Cells*, 139:95–100, August 2015. doi: 10.1016/j.solmat.2015.03.017. URL https://doi.org/10.1016/j.solmat.2015.03.017.

[12] G. Binnig, H. Rohrer, Ch. Gerber, and E. Weibel. Surface studies by scanning tunneling microscopy. *Physical Review Letters*, 49(1):57–61, jul 1982. doi: 10.1103/physrevlett.49.57. URL https://doi.org/10.1103/physrevlett.49.57.

[13] G. Binnig, C. F. Quate, and Ch. Gerber. Atomic force microscope. *Physical Review Letters*, 56(9):930–933, mar 1986. doi: 10.1103/physrevlett.56.930. URL https://doi.org/10.1103/physrevlett.56.930.

[14] S. Santos, C.-Y. Lai, T. Olukan, and M. Chiesa. Multifrequency AFM: from origins to convergence. *Nanoscale*, 9(16):5038–5043, 2017. doi: 10.1039/c7nr00993c. URL https://doi.org/10.1039/c7nr00993c.

[15] R. García and Á. San Paulo. Attractive and repulsive tip-sample interaction regimes in tapping-mode atomic force microscopy. *Physical Review B*, 60(7):4961–4967, aug 1999. doi: 10.1103/physrevb.60.4961. URL https://doi.org/10.1103/physrevb.60.4961.

[16] H.C. Hamaker. The london—van der waals attraction between spherical particles. *Physica*, 4(10):1058–1072, oct 1937. doi: 10.1016/s0031-8914(37)80203-7. URL https://doi.org/10.1016/s0031-8914(37)80203-7.

[17] V.V. Yaminsky. The hydrophobic force: the constant volume capillary approximation. *Colloids and Surfaces A: Physicochemical and Engineering Aspects*, 159(1):181–195, November 1999. doi: 10.1016/s0927-7757(99)00173-9. URL https://doi.org/10.1016/s0927-7757(99)00173-9.

[18] E.M. LIFSHITZ and M. Hamermesh. The theory of molecular attractive forces

between solids. In *Perspectives in Theoretical Physics*, pages 329–349. Elsevier, 1992. doi: 10.1016/b978-0-08-036364-6.50031-4. URL https://doi.org/10.1016/b978-0-08-036364-6.50031-4.

[19] J. N. Israelachvili. *Intermolecular and surface forces*. Academic press, 2011.

[20] R. F. Steidel et al. *An introduction to mechanical vibrations*. Wiley New York, 1979.

[21] U. Dürig, O. Züger, and A. Stalder. Interaction force detection in scanning probe microscopy: Methods and applications. *Journal of Applied Physics*, 72 (5):1778–1798, September 1992. doi: 10.1063/1.352348. URL https://doi.org/10.1063/1.352348.

[22] S.N. Magonov, V. Elings, and M.-H. Whangbo. Phase imaging and stiffness in tapping-mode atomic force microscopy. *Surface Science*, 375(2-3):L385–L391, apr 1997. doi: 10.1016/s0039-6028(96)01591-9. URL https://doi.org/10.1016/s0039-6028(96)01591-9.

[23] R. García, J. Tamayo, and Á. San Paulo. Phase contrast and surface energy hysteresis in tapping mode scanning force microsopy. *Surface and Interface Analysis*, 27(5-6):312–316, may 1999. doi: 10.1002/(sici)1096-9918(199905/06)27:5/6⟨312::aid-sia496⟩3.0.co;2-y. URL https://doi.org/10.1002/(sici)1096-9918(199905/06)27:5/6<312::aid-sia496>3.0.co;2-y.

[24] M. Tello, A. San Paulo, TR. Rodrıguez, M.C. Blanco, and R. Garcıa. Imaging cobalt nanoparticles by amplitude modulation atomic force microscopy: comparison between low and high amplitude solutions. *Ultramicroscopy*, 97(1-4): 171–175, 2003.

[25] H.-J. Butt, B. Cappella, and M. Kappl. Force measurements with the atomic force microscope: Technique, interpretation and applications. *Surface Science Reports*, 59(1-6):1–152, October 2005. doi: 10.1016/j.surfrep.2005.08.003. URL https://doi.org/10.1016/j.surfrep.2005.08.003.

[26] A. F. Payam, J. R. Ramos, and R. García. Molecular and nanoscale compositional contrast of soft matter in liquid: Interplay between elastic and dissipative interactions. *ACS Nano*, 6(6):4663–4670, May 2012. doi: 10.1021/nn2048558. URL https://doi.org/10.1021/nn2048558.

[27] R. García. Dynamic atomic force microscopy methods. *Surface Science Reports*, 47(6-8):197–301, sep 2002. doi: 10.1016/s0167-5729(02)00077-8. URL https://doi.org/10.1016/s0167-5729(02)00077-8.

[28] J. Melcher, C. Carrasco, X. Xu, J. L. Carrascosa, J. Gomez-Herrero, P. Jose de Pablo, and A. Raman. Origins of phase contrast in the atomic force microscope in liquids. *Proceedings of the National Academy of Sciences*, 106(33):13655–13660, August 2009. doi: 10.1073/pnas.0902240106. URL https://doi.org/10.1073/pnas.0902240106.

[29] D.l Platz, D. Forchheimer, E. A. Tholén, and D. B. Haviland. Interaction imaging with amplitude-dependence force spectroscopy. *Nature Communications*, 4(1), January 2013. doi: 10.1038/ncomms2365. URL `https://doi.org/10.1038/ncomms2365`.

[30] A. J. Katan, M. H. van Es, and T. H. Oosterkamp. Quantitative force versus distance measurements in amplitude modulation AFM: a novel force inversion technique. *Nanotechnology*, 20(16):165703, apr 2009. doi: 10.1088/0957-4484/20/16/165703. URL `https://doi.org/10.1088/0957-4484/20/16/165703`.

[31] S. Santos, K. Gadelrab, J. Font, and M. Chiesa. Single-cycle atomic force microscope force reconstruction: resolving time-dependent interactions. *New Journal of Physics*, 15(8):083034, aug 2013. doi: 10.1088/1367-2630/15/8/083034. URL `https://doi.org/10.1088/1367-2630/15/8/083034`.

[32] J. P. Cleveland, B. Anczykowski, A. E. Schmid, and V. B. Elings. Energy dissipation in tapping-mode atomic force microscopy. *Applied Physics Letters*, 72(20):2613–2615, may 1998. doi: 10.1063/1.121434. URL `https://doi.org/10.1063/1.121434`.

[33] J. E. Sader and S. P. Jarvis. Accurate formulas for interaction force and energy in frequency modulation force spectroscopy. *Applied Physics Letters*, 84(10):1801–1803, mar 2004. doi: 10.1063/1.1667267. URL `https://doi.org/10.1063/1.1667267`.

[34] S. Santos, C. A. Amadei, T.-C. Tang, V. Barcons Xixons, and M. Chiesa. Deconstructing the governing dissipative phenomena in the nanoscale. 2014.

[35] S. Santos, C.-Y. Lai, C. A. Amadei, K. R. Gadelrab, T.-C. Tang, A. Verdaguer, V. Barcons, J. Font, J. Colchero, and M. Chiesa. The mendeleev–meyer force project. *Nanoscale*, 8(40):17400–17406, 2016. doi: 10.1039/c6nr06094c. URL `https://doi.org/10.1039/c6nr06094c`.

[36] J.-Y. Lu, T. Olukan, S. R. Tamalampudi, A. Al-Hagri, C.-Y. Lai, M. A. A. Mahri, H.Apostoleris, I. Almansouri, and M. Chiesa. Insights into graphene wettability transparency by locally probing its surface free energy. *Nanoscale*, 11(16):7944–7951, 2019. doi: 10.1039/c9nr00155g. URL `https://doi.org/10.1039/c9nr00155g`.

[37] K. Sloyan, C.-Y. Lai, J.-Y. Lu, B. Alfakes, S. A. Hassan, I. Almansouri, M. S. Dahlem, and M. Chiesa. Discerning the contribution of morphology and chemistry in wettability studies. *The Journal of Physical Chemistry A*, 122(38):7768–7773, July 2018. doi: 10.1021/acs.jpca.8b04197. URL `https://doi.org/10.1021/acs.jpca.8b04197`.

[38] S. Santos, V. Barcons, J. Font, and N. H. Thomson. Cantilever dynamics in amplitude modulation afm: continuous and discontinuous transitions. *Journal of Physics D: Applied Physics*, 43(27):275401, 2010.

[39] S. Santos, V.Barcons, J. Font, and N. H. Thomson. Bi-stability of amplitude modulation AFM in air: deterministic and stochastic outcomes for imaging biomolecular systems. *Nanotechnology*, 21(22):225710, may 2010. doi: 10.1088/0957-4484/21/22/225710. URL https://doi.org/10.1088/0957-4484/21/22/225710.

[40] R. García and A. San Paulo. Amplitude curves and operating regimes in dynamic atomic force microscopy. *Ultramicroscopy*, 82(1-4):79–83, February 2000. doi: 10.1016/s0304-3991(99)00132-1. URL https://doi.org/10.1016/s0304-3991(99)00132-1.

[41] L. Zitzler, S. Herminghaus, and F. Mugele. Capillary forces in tapping mode atomic force microscopy. *Physical Review B*, 66(15):155436, 2002.

[42] S. Santos, L. Guang, T. Souier, K. Gadelrab, M. Chiesa, and N. H. Thomson. A method to provide rapid in situ determination of tip radius in dynamic atomic force microscopy. *Review of Scientific Instruments*, 83(4):043707, April 2012. doi: 10.1063/1.4704376. URL https://doi.org/10.1063/1.4704376.

[43] P. Gleyzes, P. K. Kuo, and A. C. Boccara. Bistable behavior of a vibrating tip near a solid surface. *Applied Physics Letters*, 58(25):2989–2991, June 1991. doi: 10.1063/1.104690. URL https://doi.org/10.1063/1.104690.

[44] C. Maragliano, A. Glia, M. Stefancich, and M. Chiesa. Effective AFM cantilever tip size: methods forin-situdetermination. *Measurement Science and Technology*, 26(1):015002, nov 2014. doi: 10.1088/0957-0233/26/1/015002. URL https://doi.org/10.1088/0957-0233/26/1/015002.

[45] J. L. Hutter and J. Bechhoefer. Calibration of atomic-force microscope tips. *Review of Scientific Instruments*, 64(7):1868–1873, jul 1993. doi: 10.1063/1.1143970. URL https://doi.org/10.1063/1.1143970.

[46] M. Chiesa and C.-Y. Lai. Surface aging investigation by means of an AFM-based methodology and the evolution of conservative nanoscale interactions. *Physical Chemistry Chemical Physics*, 20(29):19664–19671, 2018. doi: 10.1039/c8cp03454k. URL https://doi.org/10.1039/c8cp03454k.

[47] Y.-C. Chiou, T. A. Olukan, M. A. Almahri, H. Apostoleris, C. H. Chiu, C.-Y. Lai, J.-Y. Lu, S. Santos, I. Almansouri, and M. Chiesa. Direct measurement of the magnitude of the van der waals interaction of single and multilayer graphene. *Langmuir*, 34(41):12335–12343, September 2018. doi: 10.1021/acs.langmuir.8b02802. URL https://doi.org/10.1021/acs.langmuir.8b02802.

[48] Y. Martin, C. C. Williams, and H. K. Wickramasinghe. Atomic force microscope–force mapping and profiling on a sub 100-å scale. *Journal of Applied Physics*, 61(10):4723–4729, may 1987. doi: 10.1063/1.338807. URL https://doi.org/10.1063/1.338807.

[49] T. R. Albrecht, P. Grütter, D. Horne, and D. Rugar. Frequency modulation detection using high-qcantilevers for enhanced force microscope sensitivity. *Journal of Applied Physics*, 69(2):668–673, jan 1991. doi: 10.1063/1.347347. URL https://doi.org/10.1063/1.347347.

[50] Q. Zhong, D. Inniss, K. Kjoller, and V.B. Elings. Fractured polymer/silica fiber surface studied by tapping mode atomic force microscopy. *Surface Science Letters*, 290(1-2):L688–L692, June 1993. doi: 10.1016/0167-2584(93)90906-y. URL https://doi.org/10.1016/0167-2584(93)90906-y.

[51] A. San Paulo and R. García. High-resolution imaging of antibodies by tapping-mode atomic force microscopy: Attractive and repulsive tip-sample interaction regimes. *Biophysical Journal*, 78(3):1599–1605, March 2000. doi: 10.1016/s0006-3495(00)76712-9. URL https://doi.org/10.1016/s0006-3495(00)76712-9.

[52] J. Tamayo and R. García. Deformation, contact time, and phase contrast in tapping mode scanning force microscopy. *Langmuir*, 12(18):4430–4435, January 1996. doi: 10.1021/la960189l. URL https://doi.org/10.1021/la960189l.

[53] R. W. Stark. Spectroscopy of higher harmonics in dynamic atomic force microscopy. *Nanotechnology*, 15(3):347–351, December 2003. doi: 10.1088/0957-4484/15/3/020. URL https://doi.org/10.1088/0957-4484/15/3/020.

[54] M. Radmacher, M. Fritz, and P.K. Hansma. Imaging soft samples with the atomic force microscope: gelatin in water and propanol. *Biophysical Journal*, 69(1):264–270, July 1995. doi: 10.1016/s0006-3495(95)79897-6. URL https://doi.org/10.1016/s0006-3495(95)79897-6.

[55] N. Jalili and K. Laxminarayana. A review of atomic force microscopy imaging systems: application to molecular metrology and biological sciences. *Mechatronics*, 14(8):907–945, October 2004. doi: 10.1016/j.mechatronics.2004.04.005. URL https://doi.org/10.1016/j.mechatronics.2004.04.005.

[56] T. R. Rodríguez and R. García. Compositional mapping of surfaces in atomic force microscopy by excitation of the second normal mode of the microcantilever. *Applied Physics Letters*, 84(3):449–451, January 2004. doi: 10.1063/1.1642273. URL https://doi.org/10.1063/1.1642273.

[57] S. Kawai, T. Glatzel, S. Koch, B. Such, A. Baratoff, and E. Meyer. Systematic achievement of improved atomic-scale contrast via bimodal dynamic force microscopy. *Physical Review Letters*, 103(22), November 2009. doi: 10.1103/physrevlett.103.220801. URL https://doi.org/10.1103/physrevlett.103.220801.

[58] M. Deniz Aksoy and A. Atalar. Force spectroscopy using bimodal frequency

modulation atomic force microscopy. *Physical Review B*, 83(7), February 2011. doi: 10.1103/physrevb.83.075416. URL https://doi.org/10.1103/physrevb.83.075416.

[59] D. Martinez-Martin, E. T. Herruzo, C. Dietz, J. Gomez-Herrero, and R. Garcia. Noninvasive protein structural flexibility mapping by bimodal dynamic force microscopy. *Physical Review Letters*, 106(19), May 2011. doi: 10.1103/physrevlett.106.198101. URL https://doi.org/10.1103/physrevlett.106.198101.

[60] E. T. Herruzo, A. P. Perrino, and R. García. Fast nanomechanical spectroscopy of soft matter. *Nature Communications*, 5(1), January 2014. doi: 10.1038/ncomms4126. URL https://doi.org/10.1038/ncomms4126.

[61] C.-Y. Lai, S. P., S. Santos, R. Garcia, and M. Chiesa. Rapid quantitative chemical mapping of surfaces with sub-2 nm resolution. *Nanoscale*, 8 (18):9688–9694, 2016. doi: 10.1039/c6nr00496b. URL https://doi.org/10.1039/c6nr00496b.

[62] S. Santos. Enhanced sensitivity and contrast with bimodal atomic force microscopy with small and ultra-small amplitudes in ambient conditions. *Applied Physics Letters*, 103(23):231603, December 2013. doi: 10.1063/1.4840075. URL https://doi.org/10.1063/1.4840075.

[63] C.-Y. Lai, S. Santos, and M. Chiesa. Systematic multidimensional quantification of nanoscale systems from bimodal atomic force microscopy data. *ACS Nano*, 10(6):6265–6272, May 2016. doi: 10.1021/acsnano.6b02455. URL https://doi.org/10.1021/acsnano.6b02455.

[64] S. Sgouridis, M. Carbajales-Dale, D. Csala, M. Chiesa, and U. Bardi. Comparative net energy analysis of renewable electricity and carbon capture and storage. *Nature Energy*, April 2019. doi: 10.1038/s41560-019-0365-7. URL https://doi.org/10.1038/s41560-019-0365-7.

[65] B. Parida, S. Iniyan, and R. Goic. A review of solar photovoltaic technologies. *Renewable and Sustainable Energy Reviews*, 15(3):1625–1636, April 2011. doi: 10.1016/j.rser.2010.11.032. URL https://doi.org/10.1016/j.rser.2010.11.032.

[66] M. A. Green. Thin-film solar cells: review of materials, technologies and commercial status. *Journal of Materials Science: Materials in Electronics*, 18 (S1):15–19, April 2007. doi: 10.1007/s10854-007-9177-9. URL https://doi.org/10.1007/s10854-007-9177-9.

[67] M. Huang, Z. Hameiri, H. Gong, W.-C. Wong, A. G. Aberle, and T. Mueller. Novel hybrid electrode using transparent conductive oxide and silver nanoparticle mesh for silicon solar cell applications. *Energy Procedia*, 55:670–678,

2014. doi: 10.1016/j.egypro.2014.08.043. URL https://doi.org/10.1016/j.egypro.2014.08.043.

[68] S. H. Tsai, S. T. Ho, H. J. Jhuo, C. R. Ho, S. A. Chen, and Jr-Hau He. Toward high efficiency of inverted organic solar cells: Concurrent improvement in optical and electrical properties of electron transport layers. *Applied Physics Letters*, 102(25):253111, June 2013. doi: 10.1063/1.4812981. URL https://doi.org/10.1063/1.4812981.

[69] Z. Yang, T. Zhang, J. Li, W. Xue, C. Han, Y. Cheng, L. Qian, W. Cao, Y. Yang, and S. Chen. Multiple electron transporting layers and their excellent properties based on organic solar cell. *Scientific Reports*, 7(1), August 2017. doi: 10.1038/s41598-017-08613-7. URL https://doi.org/10.1038/s41598-017-08613-7.

[70] X. Sun, W. Luo, L. Chen, L. Zheng, C. Bao, P. Sun, N. Huang, Y. Sun, L. Fang, and L. Wang. Synthesis of porous al doped ZnO nanosheets with high adsorption and photodecolorizative activity and the key role of al doping for methyl orange removal. *RSC Advances*, 6(3):2241–2251, 2016. doi: 10.1039/c5ra21954j. URL https://doi.org/10.1039/c5ra21954j.

[71] M. Chiesa and C.-Y. Lai. Surface aging investigation by means of an AFM-based methodology and the evolution of conservative nanoscale interactions. *Physical Chemistry Chemical Physics*, 20(29):19664–19671, 2018. doi: 10.1039/c8cp03454k. URL https://doi.org/10.1039/c8cp03454k.

[72] J.-Y. Lu, C.-Y. Lai, I. Almansoori, and M. Chiesa. The evolution in graphitic surface wettability with first-principles quantum simulations: the counterintuitive role of water. *Physical Chemistry Chemical Physics*, 20(35):22636–22644, 2018. doi: 10.1039/c8cp03633k. URL https://doi.org/10.1039/c8cp03633k.

[73] M. Alshehhi, S. M. Alhassan, and M. Chiesa. Dependence of surface aging on DNA topography investigated in attractive bimodal atomic force microscopy. *Physical Chemistry Chemical Physics*, 19(16):10231–10236, 2017. doi: 10.1039/c7cp00160f. URL https://doi.org/10.1039/c7cp00160f.

[74] Y. J. Shin, Y. Wang, H. Huang, G. Kalon, A. T. S. Wee, Z. Shen, C. S. Bhatia, and H. Yang. Surface-energy engineering of graphene. *Langmuir*, 26 (6):3798–3802, March 2010. doi: 10.1021/la100231u. URL https://doi.org/10.1021/la100231u.

[75] R. Raj, S. C. Maroo, and E. N. Wang. Wettability of graphene. *Nano Letters*, 13(4):1509–1515, March 2013. doi: 10.1021/nl304647t. URL https://doi.org/10.1021/nl304647t.

[76] Z. Li, Y. Wang, A. Kozbial, G. Shenoy, F. Zhou, R. McGinley, P. Ireland, B. Morganstein, A. Kunkel, S. P. Surwade, L. Li, and H. Liu. Effect of airborne

contaminants on the wettability of supported graphene and graphite. *Nature Materials*, 12(10):925–931, July 2013. doi: 10.1038/nmat3709. URL https://doi.org/10.1038/nmat3709.

[77] J. Liu, C.-Y. Lai, Y.-Y. Zhang, M. Chiesa, and S. T. Pantelides. Water wettability of graphene: interplay between the interfacial water structure and the electronic structure. *RSC Advances*, 8(30):16918–16926, 2018. doi: 10.1039/c8ra03509a. URL https://doi.org/10.1039/c8ra03509a.

[78] A. Kozbial, Z. Li, J. Sun, X. Gong, F. Zhou, Y. Wang, H. Xu, H. Liu, and L. Li. Understanding the intrinsic water wettability of graphite. *Carbon*, 74:218–225, August 2014. doi: 10.1016/j.carbon.2014.03.025. URL https://doi.org/10.1016/j.carbon.2014.03.025.

[79] H. Apostoleris, S. Sgouridis, M. Stefancich, and M. Chiesa. Evaluating the factors that led to low-priced solar electricity projects in the middle east. *Nature Energy*, 3(12):1109–1114, October 2018. doi: 10.1038/s41560-018-0256-3. URL https://doi.org/10.1038/s41560-018-0256-3.

[80] B. Alfakes, J. Villegas, H. Apostoleris, R. Devarapalli, S. Tamalampudi, J.-Y. Lu, J. V., I. A., and M. Chiesa. Optoelectronic tunability of hf doped zno for photovoltaic applications, submitted.

[81] S.T. Tan, B.J. Chen, X.W. Sun, X. Hu, X.H. Zhang, and S.J. Chua. Properties of polycrystalline ZnO thin films by metal organic chemical vapor deposition. *Journal of Crystal Growth*, 281(2-4):571–576, August 2005. doi: 10.1016/j.jcrysgro.2005.04.093. URL https://doi.org/10.1016/j.jcrysgro.2005.04.093.

[82] B.P. Zhang, K. Wakatsuki, N.T. Binh, N. Usami, and Y. Segawa. Effects of growth temperature on the characteristics of ZnO epitaxial films deposited by metalorganic chemical vapor deposition. *Thin Solid Films*, 449(1-2):12–19, February 2004. doi: 10.1016/s0040-6090(03)01466-4. URL https://doi.org/10.1016/s0040-6090(03)01466-4.

[83] H. Kim, C. M. Gilmore, A. Piqué, J. S. Horwitz, H. Mattoussi, H. Murata, Z. H. Kafafi, and D. B. Chrisey. Electrical, optical, and structural properties of indium–tin–oxide thin films for organic light-emitting devices. *Journal of Applied Physics*, 86(11):6451–6461, dec 1999. doi: 10.1063/1.371708. URL https://doi.org/10.1063/1.371708.

[84] M.A. Martínez, J. Herrero, and M.T. Gutiérrez. Deposition of transparent and conductive al-doped ZnO thin films for photovoltaic solar cells. *Solar Energy Materials and Solar Cells*, 45(1):75–86, January 1997. doi: 10.1016/s0927-0248(96)00066-9. URL https://doi.org/10.1016/s0927-0248(96)00066-9.

[85] A. Gupta and A. D. Compaan. All-sputtered 14% CdS / CdTe thin-film solar

cell with zno: Al transparent conducting oxide. *Applied Physics Letters*, 85 (4):684–686, July 2004. doi: 10.1063/1.1775289. URL https://doi.org/10.1063/1.1775289.

[86] D. Kim, I. Yun, and H. Kim. Fabrication of rough al doped ZnO films deposited by low pressure chemical vapor deposition for high efficiency thin film solar cells. *Current Applied Physics*, 10(3):S459–S462, May 2010. doi: 10.1016/j.cap.2010.02.030. URL https://doi.org/10.1016/j.cap.2010.02.030.

[87] L. Shen, Z.Q. Ma, C. Shen, F. Li, Bo. He, and F. Xu. Studies on fabrication and characterization of a ZnO/p-si-based solar cell. *Superlattices and Microstructures*, 48(4):426–433, October 2010. doi: 10.1016/j.spmi.2010.08.007. URL https://doi.org/10.1016/j.spmi.2010.08.007.

[88] R. Pietruszka, B.S. Witkowski, E. Zielony, K. Gwozdz, E. Placzek-Popko, and M. Godlewski. ZnO/si heterojunction solar cell fabricated by atomic layer deposition and hydrothermal methods. *Solar Energy*, 155:1282–1288, October 2017. doi: 10.1016/j.solener.2017.07.071. URL https://doi.org/10.1016/j.solener.2017.07.071.

[89] A. K. Sharma, J. Narayan, J. F. Muth, C. W. Teng, C. Jin, A. Kvit, R. M. Kolbas, and O. W. Holland. Optical and structural properties of epitaxial MgxZn1-xO alloys. *Applied Physics Letters*, 75(21):3327–3329, November 1999. doi: 10.1063/1.125340. URL https://doi.org/10.1063/1.125340.

[90] T. Minemoto, Y. Hashimoto, T. Satoh, T. Negami, H. Takakura, and Y. Hamakawa. Cu(In, Ga)Se2 solar cells with controlled conduction band offset of window/Cu(In, Ga)Se2 layers. *Journal of Applied Physics*, 89(12):8327–8330, June 2001. doi: 10.1063/1.1366655. URL https://doi.org/10.1063/1.1366655.

[91] R. Pietruszka, R. Schifano, T.A. Krajewski, B.S. Witkowski, K. Kopalko, L. Wachnicki, E. Zielony, K. Gwozdz, P. Bieganski, E. Placzek-Popko, and M. Godlewski. Improved efficiency of n-ZnO/p-si based photovoltaic cells by band offset engineering. *Solar Energy Materials and Solar Cells*, 147:164–170, April 2016. doi: 10.1016/j.solmat.2015.12.018. URL https://doi.org/10.1016/j.solmat.2015.12.018.

[92] D. J. Cohen, K. C. Ruthe, and S. A. Barnett. Transparent conducting zn1-xMgxO:(al, in) thin films. *Journal of Applied Physics*, 96(1):459–467, July 2004. doi: 10.1063/1.1760239. URL https://doi.org/10.1063/1.1760239.

[93] K. Matsubara, H. Tampo, H. Shibata, A. Yamada, P. Fons, K. Iwata, and S. Niki. Band-gap modified al-doped zn1-xMgxO transparent conducting films deposited by pulsed laser deposition. *Applied Physics Letters*, 85(8):1374–1376, August 2004. doi: 10.1063/1.1784544. URL https://doi.org/10.1063/1.1784544.

[94] C. Hyoun Ahn, J. Hyun Kim, and H. Koun Cho. Tunable electrical and optical properties in composition controlled hf:ZnO thin films grown by atomic layer deposition. *Journal of The Electrochemical Society*, 159(4):H384–H387, 2012. doi: 10.1149/2.026204jes. URL https://doi.org/10.1149/2.026204jes.

[95] Y. Geng, Z.-Y. Xie, W. Yang, S.-S. Xu, Q-Q. Sun, S.-J. Ding, H.-L. Lu, and D. W. Zhang. Structural, optical, and electrical properties of hf-doped ZnO films deposited by atomic layer deposition. *Surface and Coatings Technology*, 232:41–45, October 2013. doi: 10.1016/j.surfcoat.2013.04.050. URL https://doi.org/10.1016/j.surfcoat.2013.04.050.

[96] J. Lim and C. Lee. Effects of substrate temperature on the microstructure and photoluminescence properties of ZnO thin films prepared by atomic layer deposition. *Thin Solid Films*, 515(7-8):3335–3338, February 2007. doi: 10.1016/j.tsf.2006.09.007. URL https://doi.org/10.1016/j.tsf.2006.09.007.

[97] H. Saarenpää, T. Niemi, A. Tukiainen, H. Lemmetyinen, and N. Tkachenko. Aluminum doped zinc oxide films grown by atomic layer deposition for organic photovoltaic devices. *Solar Energy Materials and Solar Cells*, 94(8):1379–1383, August 2010. doi: 10.1016/j.solmat.2010.04.006. URL https://doi.org/10.1016/j.solmat.2010.04.006.

[98] R. Gaillac, P. Pullumbi, and F.-X. Coudert. ELATE: an open-source online application for analysis and visualization of elastic tensors. *Journal of Physics: Condensed Matter*, 28(27):275201, May 2016. doi: 10.1088/0953-8984/28/27/275201. URL http://progs.coudert.name/elate/mp?mp-2133.

[99] G.S. Rohrer. The anisotropy of metal oxide surface properties. In *Oxide Surfaces*, pages 485–513. Elsevier, 2001. doi: 10.1016/s1571-0785(01)80032-8. URL https://doi.org/10.1016/s1571-0785(01)80032-8.

[100] C. Tian, Q. Zhang, A. Wu, M. Jiang, Z. Liang, B. Jiang, and H. Fu. Cost-effective large-scale synthesis of ZnO photocatalyst with excellent performance for dye photodegradation. *Chemical Communications*, 48(23):2858, 2012. doi: 10.1039/c2cc16434e. URL https://doi.org/10.1039/c2cc16434e.

[101] I. V. Tudose and M. Suchea. ZnO for photocatalytic air purification applications. *IOP Conference Series: Materials Science and Engineering*, 133:012040, June 2016. doi: 10.1088/1757-899x/133/1/012040. URL https://doi.org/10.1088/1757-899x/133/1/012040.

[102] T. S. Moss. The interpretation of the properties of indium antimonide. *Proceedings of the Physical Society. Section B*, 67(10):775–782, October 1954. doi: 10.1088/0370-1301/67/10/306. URL https://doi.org/10.1088/0370-1301/67/10/306.

[103] E. Burstein. Anomalous optical absorption limit in InSb. *Physical Review*,

93(3):632–633, February 1954. doi: 10.1103/physrev.93.632. URL https://doi.org/10.1103/physrev.93.632.